

<https://doi.org/10.1038/s44306-024-00070-z>

# Emerging ferromagnetic materials for electrical spin injection: towards semiconductor spintronics



Yufang Xie<sup>1,2</sup>, Su-Yun Zhang<sup>1</sup>, Yin Yin<sup>3</sup>, Naihang Zheng<sup>1</sup>, Anwar Ali<sup>1</sup>, Muhammad Younis<sup>1</sup>,  
Shuangchen Ruan<sup>1</sup> & Yu-Jia Zeng<sup>1</sup> ✉

Spintronics is a promising field beyond complementary metal-oxide semiconductors technology. It presents a unique approach to diminishing the energy consumption of memory and logic devices by utilizing spin. The proposed influential memory and logic device is the spin transistor. However, limited spin injection efficiency from the metallic ferromagnetic electrode into the semiconductor layer has been a major obstacle for the advances of spin transistors. Three key properties are critical for magnetic materials in future spintronic devices to improve the spin injection efficiency, namely high spin polarization, robust room-temperature ferromagnetism, and comparable resistance with the semiconductor. Considering these factors, we will explore four major categories of ferromagnetic materials: Heusler alloys, dilute magnetic semiconductors, Si- or Ge-based intermetallic compounds, and two-dimensional ferromagnets. We present a comprehensive overview of the significant milestones for each type of material in terms of their property improvements, functionality achievements, and fundamental applications for spintronics. Finally, we will briefly address the challenges which need to be tackled for practical application in memory and logic devices.

Conventional silicon-based metal-oxide-semiconductor (MOS) devices, which relying on manipulating electron's charge (specifically one degree of freedom of electrons) are confronted with the significant challenges in miniaturizing of electronic devices due to the fundamental physical limits<sup>1</sup>. The exploration of advanced information technology with low-energy consumption and high-speed operation, which complements the existing silicon-based complementary metal-oxide semiconductors (CMOS) technology, is urgently required. Many strategies have already been proposed, such as nanoelectronics, molecular electronics, valley electronics, spintronics, and quantum information technologies<sup>1,2</sup>. Among these, spintronics, which exploits the spin degree instead of the charge degree for electrons or holes, has the potential to become an innovative pathway beyond physical limits and satisfy the speed and energy-efficiency needs of the emerging computing paradigm<sup>3</sup>.

Spintronics is a multidisciplinary field focused on effectively utilizing spin degrees of freedom in solid-state systems<sup>3,4</sup>. The term spin refers to either the spin of a single electron, which is characterized by a quantized angular momentum of  $m_s\hbar$  (where  $m_s = \pm 1/2$  represents the spin magnetic quantum number), or the average spin of a group of electrons as evidenced

by their magnetization. The quantized spin angular momentum of electrons exists in two distinct states: spin down  $\downarrow$  (minority-spin) and spin up  $\uparrow$  (majority-spin). Spintronics devices are built based on the comprehensive utilization of the spin degree of freedom in certain functional units, such as spin valve, magnetic tunnel junctions (MTJs), spin transfer torque (STT), spin-orbit torque (SOT) and spin field effect transistor (spin-FET). Their structure diagrams are depicted in Fig. 1. These prototypes, even commercial successful spin functionality units, involve a wide coverage of fascinating spin physics, namely injection, transmission, detection, and even manipulation of spins<sup>3</sup>. Importantly, the injection, transmission and detection of spin degree during the whole operation for a certain spin-based unit governs the success and endurance of ultimate spintronics performance. During this procedure, spin population, coherence and collection should be seriously considered. As for the spin manipulation, the extra driving force from either orbital momentum inter-coupling or external physical stimuli works essentially. This, in turn, creates more possibilities for controlling and tailoring spin activity in addition to simple transmission.

The milestone discovery of the giant magnetoresistance (GMR) effect within metallic multilayers (Fig. 1a) in 1988 undoubtedly validated the

<sup>1</sup>Key Laboratory of Optoelectronic Devices and Systems of Ministry of Education and Guangdong Province, College of Physics and Optoelectronic Engineering, Shenzhen University, Shenzhen, 518060, PR China. <sup>2</sup>School of Physics and Electronic Engineering, Jiangsu University, 212013 Zhenjiang, China. <sup>3</sup>School of Materials Science and Engineering, Jiangsu University, 212013 Zhenjiang, China. ✉e-mail: [yjzeng@szu.edu.cn](mailto:yjzeng@szu.edu.cn)

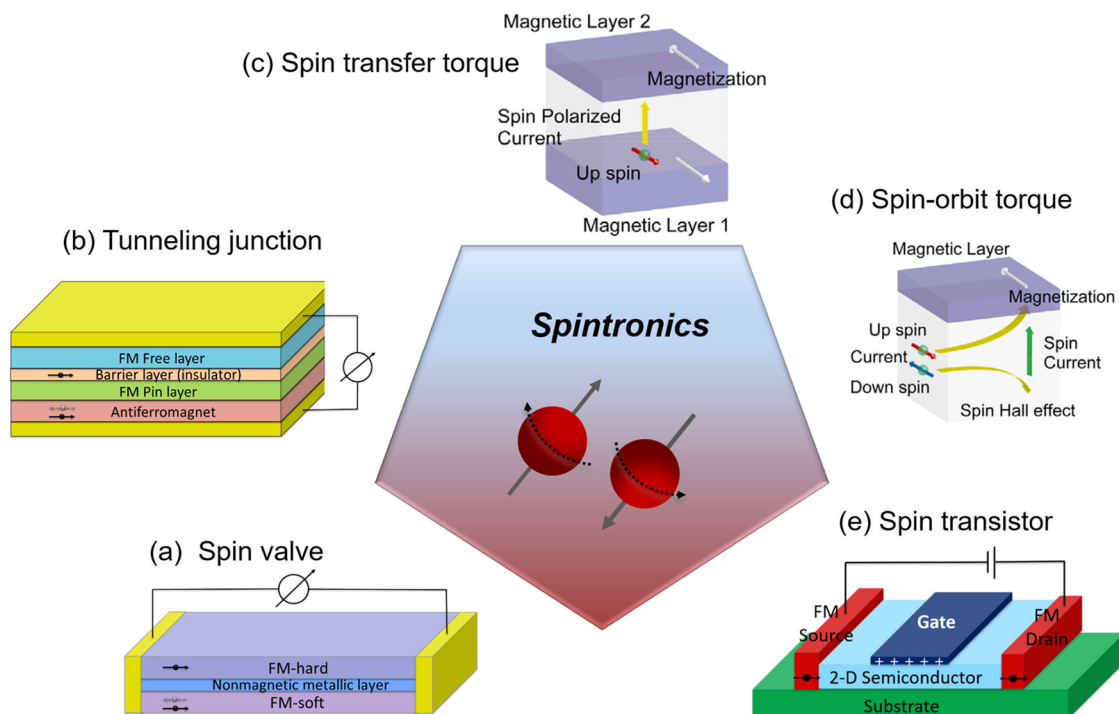


**Fig. 1 | The milestone discovery of spintronics.** Schematic of (a) spin valve structure based on the giant magnetoresistance effect; (b), magnetic tunnel junction structure based on the tunneling magnetoresistance effect; (c), spin transfer torque

switching; (d), spin orbit torque switching and (e) the Datta and Das spin transistor. Images of c and d are reprinted with permission from ref. 9 Copyright 2020 Wiley Periodicals, Inc.

detectable coupling between charge and spin, which greatly revolutionized the spintronics industry by successful application in Hard Disk Drives (HDD)<sup>5,6</sup>. Soon, in 1991, the GMR spin valve was designed by Dieny, which is composed of an additive pinning layer with one ferromagnetic (FM) layer while the other FM layer is free. This valve geometry works efficiently in improving magnetic field sensitivity for HDD that use GMR as read heads. Afterward, in 1995, the introduction of insulating barrier amorphous alumina between counter FM electrodes (Fig. 1b), which demonstrated a large reproducible magnetoresistance signal, marked the tunneling magnetoresistance (TMR) effects<sup>7</sup> started to play a critical role in spintronics industry. The TMR signal was improved by over 600% once the single crystal MgO was selected as the insulating barrier<sup>8</sup>. The ultrahigh TMR signal not only expands the hard disk recording but also encourages the advancement of magnetoresistive random access memory (MRAM). The recent confirmation of STT (Fig. 1c)<sup>9</sup> and SOT (Fig. 1d)<sup>10</sup> effects have made MTJs more worthwhile for the blossom of low-power and high-density data storage.

As just illustrated, the development of GMR and TMR devices is closely linked to optimizing both metals and insulators under the frame of two-terminal geometry. Semiconductor, which possess unique advantage of gate tunable carrier density, affords distinctive advantage in spin information storage and spin logic computing<sup>11</sup>. This emerging field has sparked significant scientific interests and high expectations for the development of innovative devices that can convert spin information into an electrical signal, and vice versa. One of the primary objectives of semiconductor-based spintronics is to achieve the realization of a three-terminal device known as the spin-FET, as depicted in Fig. 1e. Spin-FETs offer non-volatile storage, energy efficient and quicker operation than conventional transistors<sup>11</sup>. More importantly, this device holds significant potential for realizing nonvolatile memory and amplification functionalities within a single unit. However, such devices confront substantial problems including ineffective spin injection from the FM source into the channel and relaxation of spin in the channel which significantly deteriorate the devices' performance<sup>12–15</sup>. This stands in clear contrast to the conservation of electron charge. Hence, there are still challenges to be addressed in the implementation of such spintronic

devices. In this regard, the effective spin injection from FM source into semiconductor channel is of both fundamental and technological importance, making it a crucial solution to be achieved.

This review aims to provide a comprehensive summary of the burgeoning field of electrical spin injection from the perspectives of materials, performances, and applications. After this brief overview of spintronics concepts and developments in section 1, we illustrate the challenges during the electrical spin injection within FM/semiconductor heterostructure in section 2. Section 3 summarizes the FM materials used as spin source/drain. Different types of FM material systems, including Co-based Heusler alloy, dilute magnetic semiconductor  $\text{Ga}_{1-x}\text{Mn}_x\text{As}$ , Si- or Ge-based intermetallic compounds  $\text{Mn}_5\text{Ge}_3$ , and two-dimensional (2D) materials, are discussed based on the magnetic and electronic properties which are applicable to the highly efficient spin injection at room temperature (RT). Finally, we conclude by discussing the future challenges and opportunities for the development of spintronics-based nonvolatile logic-in-memory applications.

## Issues and solutions of electrical spin injection in ferromagnet/semiconductor heterostructures

The successful implementation of a spin-FET (Fig. 1e) relies on achieving the following fundamental functionalities<sup>3,12–15</sup>: (i) spin injection/extraction into/from a semiconductor channel and (ii) spin-dependent transport via a semiconductor channel. A proposed influential semiconductor-based device is the Datta-Das transistor<sup>16</sup>. It features a FET-like structure, with FM metallic contacts (e.g.,  $\text{Ga}_{1-x}\text{Mn}_x\text{As}$ ) and a non-ferromagnetic semiconductor channel, as illustrated in Fig. 1e. The polarized spins are injected into a 2D electron-gas channel, for example GaAs, where the transport of the polarized spin current is supposed to be ballistic. They are exposed to an electrical field controlled by the gate, which in turn induces an effective Rashba magnetic field for manipulating electrons at a specific velocity. The electrons undergo Larmor precession during this process, and the manipulation of the spin precession angle is achieved through the effective Rashba field. The majority spins' orientations will be aligned by the gate bias to either the parallel or antiparallel direction with the FM contacts'

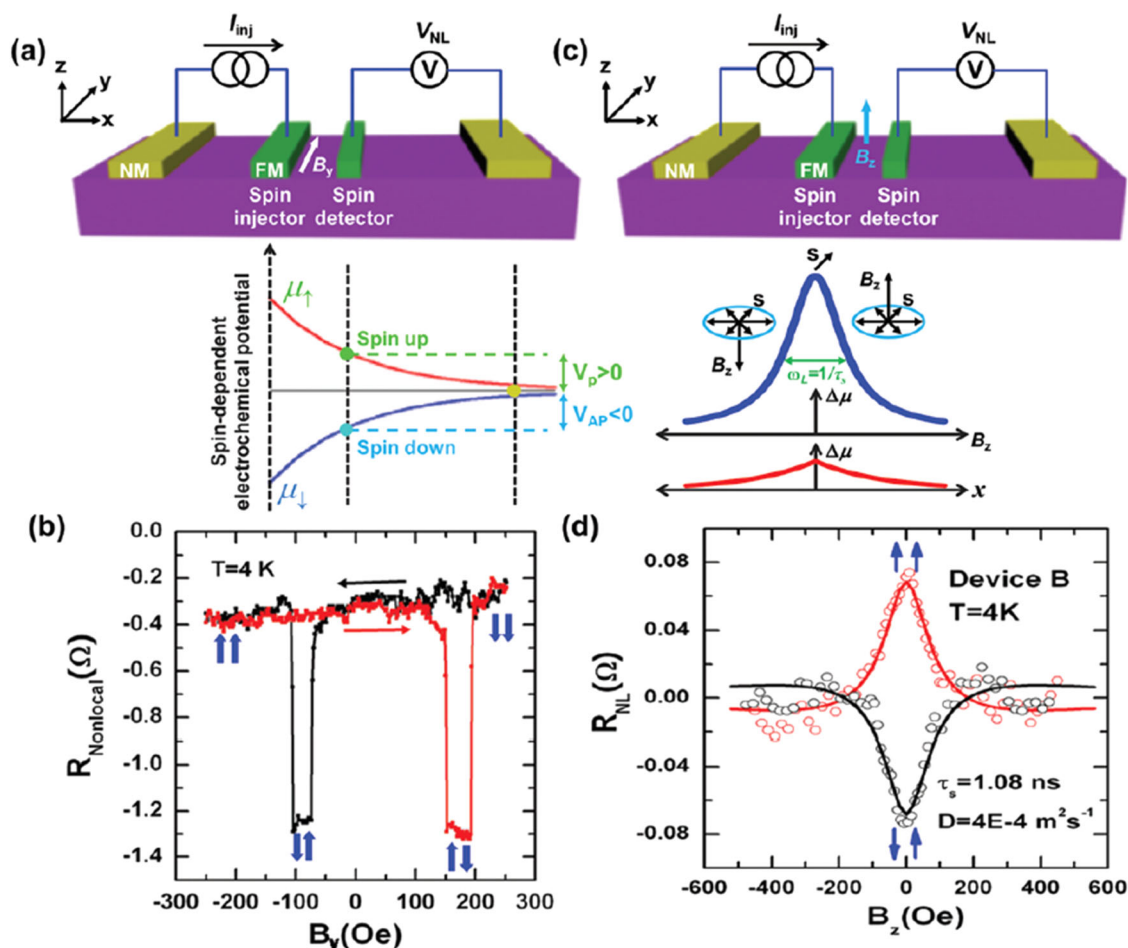


**Fig. 2 | Nonlocal SV and Hanle measurements.** **a** Illustrated in the schematic is the nonlocal measurement of spin voltage, wherein an in-plane magnetic field is applied along the easy axis of the FM spin injector and detector. **b** Characteristic nonlocal SV signals observed in n-Ge at 4 K. The sweeping direction of the magnetic field is indicated by the black and red arrows, while the relative magnetization directions of

the spin injector and detector are denoted by the blue arrows; **c** Simplified illustration of nonlocal Hanle measurement with an out-of-plane magnetic field applied perpendicular to the FM/semiconductor interface. **d** Distinctive nonlocal Hanle precession signals were observed in n-Ge at 4 K. The figures are reprinted with permission from ref. 19 Copyright 2015 by the Royal Society of Chemistry.

magnetization, resulting in correspondingly high or low conductance. It is evident that the spintronic ferromagnet/semiconductor heterostructures play a pivotal role in governing the behavior and performance of devices.

Spin signals have been detected or generated through various means, including electrical, optical, and thermal methods. The spin signals generated and detected via electrical methods, also known as spin-charge conversion, are in harmony with the electric charge operations inherent in CMOS-based integrated circuits. Suppose the efficient spin electrical injection from FM sources into the semiconductor is realized, a spin accumulation signal in the semiconductor can be electrically detected via a change in resistance or potential using Hanle effect measurement or nonlocal SV measurements<sup>17–19</sup>. Schematic illustration and typical signal results of nonlocal spin valve and Hanle measurements are displayed in Fig. 2a–d, respectively. Typically, the 3-terminal configuration was utilized, with a single FM contact serving as the spin injector and detector. Nevertheless, the 3-terminal geometry is more susceptible to spurious signals, such as Hall or anisotropic magnetoresistance effects, due to the presence of a non-zero charge current at the detector junction. To completely eliminate the possibility of spurious signal, the nonlocal 4-terminal spin transport devices (Fig. 2) are proposed. A spin detection electrode is strategically positioned outside the path of the charge current within this device, thereby furnishing precise insights into spin lifetime and spin polarization in the semiconductor channel.

As previously mentioned, spins effectively transfer from a FM source into the semiconductor, creating a significant (nonequilibrium) spin

polarization of the carriers in the semiconductor. This is a key step in demonstrating many novel spin-FETs. It's notable that the spin-polarized current in a spin-FET is typically introduced from the FM metal into the semiconductor layer via the diffusive transport through an ohmic contact. The current polarization at the FM metal/semiconductor interface is determined by<sup>14</sup>:

$$P = \frac{P_0}{1 + (1 - P_0^2) \frac{\sigma_F \lambda_{SC}}{\sigma_{SC} \lambda_F}} \quad (1)$$

where  $P_0$  represents the polarization at the Fermi level within the ferromagnet;  $\sigma_F$  and  $\sigma_{SC}$  denote the conductivity of the FM and semiconductor layer, respectively; additionally,  $\lambda_F$  and  $\lambda_{SC}$  indicate the mean free path travelled by spin carriers before undergoing a spin flipping scattering.

Based on this formula, the restricted spin injection efficiencies have predominantly been ascribed to the following factors, including the limited spin polarization  $P_0$  of electrons within the FM metallic electrodes, the conductivity mismatch problem ( $\sigma_F \gg \sigma_{SC}$ )<sup>14</sup> between the FM electrodes and the semiconductor channel, and the spin transport distance in the channel determined by the semiconductor's channel length and diffusion profile. Among them, the conductivity mismatch, that refers to the conductivity of the FM metal being approximately  $10^3$  times larger than the semiconductor channel<sup>14</sup>, strictly limit the efficient spin injection into the semiconductor considering nearly identical drop in the electrochemical potentials over the spin-up and spin-down electrons channel. To realize such spintronic

devices, it is essential to achieve efficient spin injection into semiconductors and further to effectively manipulate the spin transport in them. First, the electrical spin injection and transport in a broad range of semiconductors have been extensively investigated to seek semiconductor materials with long spin lifetime and spin diffusion length<sup>19</sup>. Second, to achieve optimal spin injection efficiency, one proposed approach involves the exploration of new materials that demonstrate a significant carrier spin polarization<sup>16,20</sup>. Potential candidates including FM oxides and associated Co<sub>2</sub>-based Heusler compounds, many of which are anticipated to exhibit “half-metallic” behavior (such as Fe<sub>3</sub>O<sub>4</sub> and Co<sub>2</sub>MnSi). Such ferromagnets are theoretically expected to have 100% spin polarization at the Fermi level arising from their unique band structure. The valence band for the majority spin ↑ is partially filled, indicating a metallic property, while there exists a gap in the density of states (DOS) for the minority spin ↓, suggesting a semiconducting behavior.

Third, it is essential to solve the “conductivity mismatch” issue and thus achieve optimal spin-injection efficiency. One potential solution involves utilizing FM electrodes that have a resistivity almost equivalent to that of the semiconductor channel, such as diluted magnetic semiconductors Ga<sub>1-x</sub>Mn<sub>x</sub>As electrodes with a GaAs transport channel<sup>21,22</sup>. Another potential solution involves inserting a spin-dependent interface resistance form a Schottky barrier or tunnel barrier<sup>23,24</sup>. The Schottky barrier has been experimentally demonstrated using direct FM/semiconductor contacts, such as Fe<sub>3</sub>Si/Si or Mn<sub>5</sub>Ge<sub>3</sub>/Ge heterojunction<sup>25–28</sup>. In this case, the in-situ germanidation or silicidation process of fabricating Fe<sub>3</sub>Si or Mn<sub>5</sub>Ge<sub>3</sub> layer is favorable for achieving atomically smooth interfaces and thus minimizing Fermi level pinning and defect-induced interface states. The tunneling barrier can be established through a sandwich structure of FM metal/insulator/semiconductor layer, as shown in Fig. 1b. An intermediate thin insulator layer (such as MgO or Al<sub>2</sub>O<sub>3</sub>) effectively serves to modulate the height of the Schottky barrier<sup>24</sup>. However, it is challenging to fabricate a superior tunneling oxide that is devoid of pinholes or defects to mitigate the phenomenon of Fermi level pinning. Until recently, the tunneling heterostructures based on 2D van der Waals (vdW) layers such as Co/MgO/MoS<sub>2</sub>, Co/TiO<sub>2</sub>/black phosphorous, and Fe<sub>3</sub>GeTe<sub>2</sub>/h-BN/Fe<sub>3</sub>GeTe<sub>2</sub> have been reported with improved interfaces and consequently exhibited superior injection performance<sup>29–31</sup>.

## Ferromagnetic materials for electrical spin injection

Spin injection, transport, and detection in ferromagnet/semiconductor heterostructures are crucial for integrating spintronic devices into current production technologies and advancing semiconductor electronics beyond their physical limits. Attaining a high level of spin injection efficiency from FM into semiconductors is an indispensable step for developing spintronic devices. For efficient spin injection, it expects a material that not only possesses high Curie temperature ( $T_C$ ) and substantial spin polarization, but also seamlessly integrates with existing Si-based CMOS technology. In this section, we will discuss various systems: FM materials with high spin polarization (e.g., half-metallic Heusler alloys Co<sub>2</sub>MnGa); FM material with matched conductivity with the semiconductor channel (e.g., dilute FM semiconductor Ga<sub>1-x</sub>Mn<sub>x</sub>As); a controllable interface between the FM electrodes and the spin transport channel coupled with a Schottky barrier that fulfills the desired interface resistance criteria (for example Si- or Ge-based intermetallic compounds Mn<sub>5</sub>Ge<sub>3</sub> on Ge substrates); and 2D vdW heterostructures consisting of 2D FM injector and 2D spin transport channels with improved interfaces for enhanced efficiency of injecting spin.

## Half-metallic Heusler alloy

Half-metallic ferromagnets (HMF) represent a promising category of materials that have garnered significant interest for their potential application as spin injectors<sup>32,33</sup>. Extensive researches have been conducted on typical half-metallic materials, particularly in ternary Heusler alloys with the composition of X<sub>2</sub>YZ or XX'YZ (full Heusler as shown in Fig. 3a) or XYZ (Half Heusler as shown in Fig. 3b). These alloys consist of transition metals (TMs) as X and Y, and group III or IV elements as Z, forming a vast collection of over 1500 compounds<sup>33</sup>. The constituent atoms were arranged

in an L21-type structure as depicted in Fig. 3a, b. The perfect crystal structure can be conceptualized as a zinc blende-type sublattice constructed by one X and one Z atom while another X atom occupy the remaining tetrahedral hole and Y atom locate in the octahedral hole. In general, half-metallic materials are magnetic due to the contribution of magnetic moments from transition metal atoms. The bonding in these compounds is sufficiently intricate to enable the opening of a gap in the minority spins' DOS, which is an essential condition for achieving half metallicity.

In this section, we will present a selection of representative compounds known as Co<sub>2</sub>YZ, including but not limited to Co<sub>2</sub>MnSi, Co<sub>2</sub>FeSi, and Co<sub>2</sub>MnGe. The synthesis and investigation of these Co-based compounds have been ongoing since the 1970s<sup>34</sup>. It is widely studied that the Co<sub>2</sub>YZ's magnetic properties adhere to the Slater-Pauling rule which accurately predicts their overall spin magnetic moment<sup>35–37</sup>. The magnetic moment ( $m$ ) per formula unit can be expressed as  $m = V_E - 24$ , where  $V_E$  represents the total valence electrons number, encompassing the summation of s and d electrons for transition metals, and s and p electrons for main group elements. As depicted in Fig. 3c, the magnetic moment of full-Heusler materials generally exhibits a linear relationship with the number of valence electrons, with only a few exceptions. Moreover, the majority of these compounds exhibit magnetic moments that are either integer or close to integer values. Furthermore, the  $T_C$  of Co<sub>2</sub>-based Heusler compounds exhibits a direct correlation with the magnetic moment. Owing to the Slater Pauling behavior of the magnetic moment (as depicted in Fig. 3d),  $T_C$  also linearly depends on the number of valence electrons, as illustrated in Fig. 4a. However, this linear tendency is disrupted for materials with 27 valence electrons. These materials, which do not exhibit magnetism, demonstrate superconductivity. Theoretical investigations<sup>35,37</sup> have revealed that the magnetic moments at the Co and Y sites exhibit a simultaneous rise with  $V_E$ , resulting in nonlinearity with  $m$ . Supposed alterations in the average Heisenberg exchange were to counterbalance the magnetic moments, a linear correlation with  $V_E$  would become apparent.

Based on the plot depicted in Fig. 4a, it is evident that  $T_C$  exhibits its highest values in half-metallic compounds with a large magnetic moment or those with a high valence electron concentration as contrasted with the predictions of the Slater-Pauling rule. The theoretical estimation for  $T_C$  reach 1185 K in compounds with 6  $\mu_B$  which corresponds to 30 valence electrons per unit cell. Co<sub>2</sub>FeSi is widely recognized as the Heusler compound with the highest magnetic moment of 5.97  $\mu_B$  at 5 K and the most elevated  $T_C$  reaching 1100 K<sup>38</sup>.

The most prominent feature of Co<sub>2</sub>YZ lies in the highest polarization which can be attributed to intricate half-metallic band structure that resides near the Fermi level<sup>39,40</sup>. The Slater-Pauling behavior is widely recognized as indicative of bulk half-metallicity (100% spin polarization). This phenomenon arises from a metallic spin-polarized band, which is determined by the valence electrons number<sup>40</sup>. Fig. 4b displays the spin-projected DOS of Co<sub>2</sub>MnZ and partial DOS plots of Co<sub>2</sub>MnGa. The DOS in FM is divided into minority and majority states due to the exchange interaction between Co and Mn atoms. The Fermi level is populated by one spin-band and resides within the bandgap of the other spin-band; thereby achieving the visualization of half-metallicity.

The transport properties are governed by electrons residing on the Fermi surface or within an energy  $eV_b$  of the Fermi level particularly applying a bias voltage of  $V_b$ . A comprehensive definition of polarization  $P(n)$  under low bias can be formulated as follows<sup>37</sup>:

$$P(n) = \frac{v_F^\uparrow D_\uparrow - v_F^\downarrow D_\downarrow}{v_F^\uparrow D_\uparrow + v_F^\downarrow D_\downarrow} \quad (2)$$

where  $v_F$  represents the Fermi velocity,  $D_\uparrow$  and  $D_\downarrow$  denote the DOS of the majority (spin-up) and minority (spin-down) spin at the Fermi level. The exponent  $n$  takes on different values depending on the specific conditions: 0 for electrons ejected in spin-polarized photoemission, 1 for ballistic transport and 2 for diffusive transport or tunneling at low bias. It is



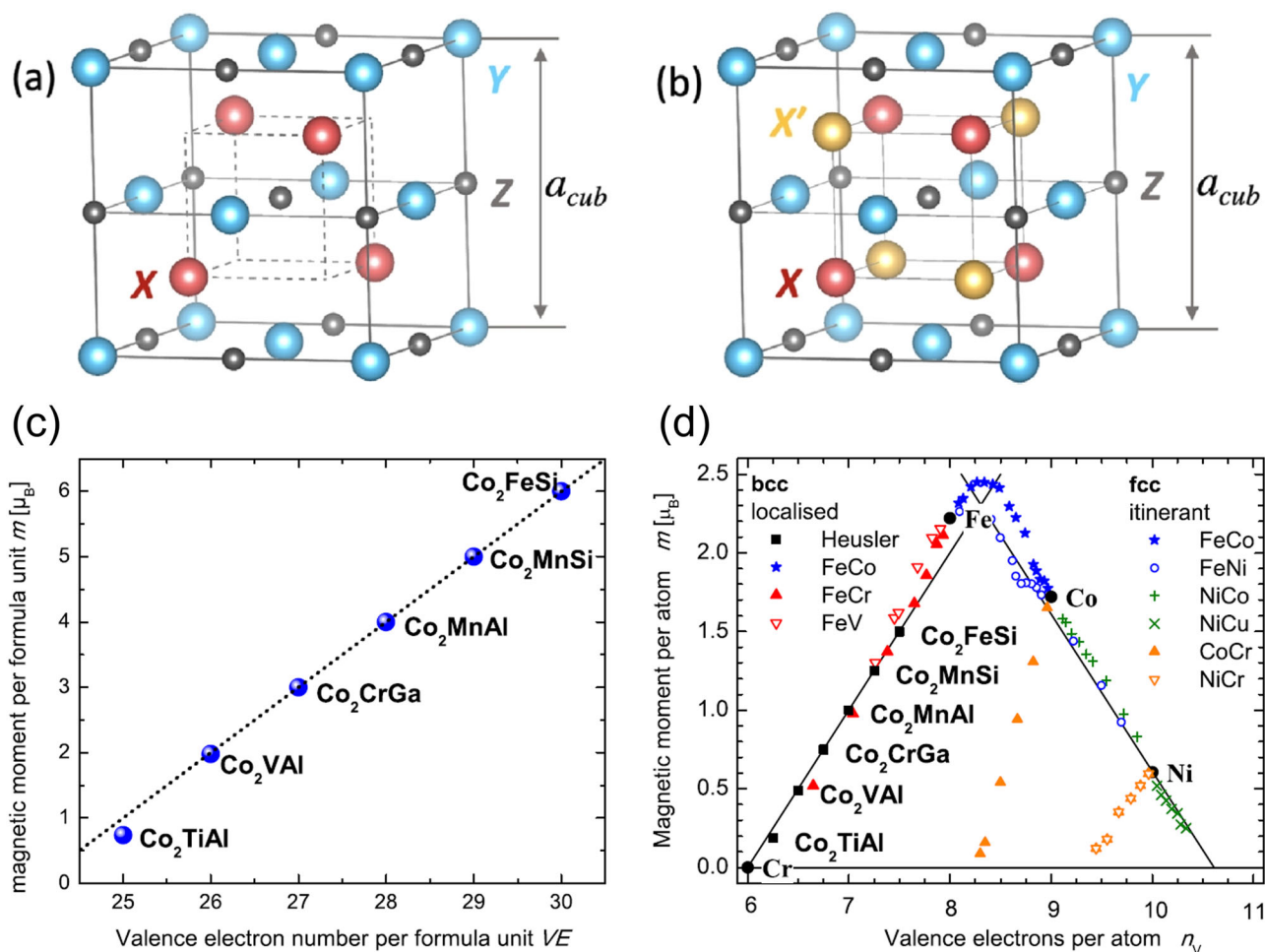


**Fig. 3 | The crystalline structure and magnetic moment of Heusler compounds.** Schematic structures of (a) half Heusler (XYZ) and (b) quaternary full Heusler (XX'YZ) compounds. c The magnetic moment per formula unit of  $Co_2$ -based Heusler compounds is in direct proportion to the number of valence electrons. This

relationship follows the Slater-Pauling curve as illustrated in d. The values of 3 d transition metals and their alloys are provided for contrast. Figures (a, b) reprinted with permission from ref. 33 Copyright 2021 by Elsevier B.V. Figures (c, d) are reprinted with permission from ref. 35 Copyright 2011 by Elsevier Ltd.

theoretically expected that conduction electrons in HMF exhibit 100% spin polarization below  $T_C$  on the basis of the polarization definition. This remarkable characteristic renders HMF ideal candidates as spin injector layers in next-generation spintronic devices.

It's notable the distinctive physical properties of Co-based Heusler alloys are dependent on the crystal structure. For instance, the half metallicity observed in Heusler-alloy films is particularly sensitive to crystal disorder, such as atomic displacement, misfit dislocation, and symmetry break near the surface of the films<sup>37,41</sup>. As previously mentioned, within the perfect lattice of  $Co_2YZ$ , one Co and Z atoms constitute a zinc blende-type sublattice, while the second Co occupies the tetrahedral voids and Y is situated in the octahedral interstices. When the Y and Z atoms interchange their places (Y-Z disorder), resulting in Y-Z disorder, and eventually the alloy undergoes a transformation into the B2 phase. Furthermore, the presence of X-Y and X-Z disorder ultimately culminates in the emergence of the A2 phase. The anti-site disorder alters the termination of film and consequently diminishes the HMF property in Heusler alloys, leading to a decrease in spin polarization.

Controlling the stoichiometry of Heusler alloy films presents a formidable challenge, often leading to deviations from the anticipated physical properties due to a deficiency or excess of specific atom species<sup>42,43</sup>. Furthermore, non-ferromagnetic interfaces have been found to be detrimental for spin injection in some Co-based Heusler alloy films<sup>13</sup>. Consequently, the measured transport spin polarization of certain Heusler alloy films has been regrettably low. For example,  $P(n)$  was found to be 58% in NiMnSb<sup>44</sup> at 4.2 K

as determined by point contact Andreev reflection.  $P(n)$  of  $Co_2MnSi$  at 10 K was demonstrated as 61% via Julliere's formula<sup>45</sup> which still exceeds that of conventional transition metals.

The diminished spin polarization of the HMF may stem from a confluence of the aforementioned factors. Currently, these FM alloys still exhibit lower spin injection efficiencies while the theoretical prediction suggests that the spin injection efficiency for HMF can potentially reach 100%. The experimentally lower efficiency of spin injection in these FM alloys can be attributed to issues such as disorder in crystal structure, non-stoichiometry, and non-ferromagnetic interfaces.

### Dilute magnetic semiconductors

The exploration of FM semiconductors has long been appealing owing to their potential applications in spintronics and their seamless integration into semiconductor devices<sup>16</sup>. The research on FM semiconductors can be traced back to the 1960s, when typical materials including europium chalcogenides (such as EuS, EuO) and chromium spinels ( $CdCr_2Se_4$ ), where magnetic elements were arranged periodically in the lattice<sup>16</sup>. The antiferromagnetic super-exchange in EuO is effectively counterbalanced by direct  $d-f$  FM exchange between neighboring Eu ions, leading to a resultant  $T_C = 68$  K<sup>47</sup>. Moreover, they demonstrate exceptional physical characteristics, such as a remarkable giant negative magnetoresistance, due to the exchange interaction between band carriers and localized spins. The  $s-d(f)$  coupling between spins of itinerant  $s$ - and localized  $d(f)$ -electrons of Eu ions leads to a significant spin splitting of the bands below  $T_C$ , as well as magnetization

fluctuations near the  $T_C$  induced by the band carriers<sup>46,48,49</sup>. Nevertheless, the low TC ( $< 100$  K, far below RT) has constrained their practical application in spintronics.

During the 1990s, the revelation of ferromagnetism ( $T_C \sim 110$  K) in III-V-based dilute magnetic semiconductors  $\text{Ga}_{1-x}\text{Mn}_x\text{As}$ <sup>50</sup> sparked significant interest among researchers. It is worth noting that GaAs possesses a zinc

blende structure, as depicted in Fig. 5a. The substitution of Mn atoms ( $\text{Mn}_{\text{Ga}}$ ) in GaAs acts as acceptors, inducing the magnetism mediated by holes. The FM interaction in this material is dependent on the p-d coupling between localized spins and hole carriers, as well as significant spin-orbit interactions in p-like orbitals that form the valence band<sup>51–53</sup>. It implies that the manifestation of  $\text{Ga}_{1-x}\text{Mn}_x\text{As}$ 's ferromagnetism is heavily reliant on the concentration of holes. In the subsequent study,  $T_C$  of  $\text{Ga}_{1-x}\text{Mn}_x\text{As}$  was empirically demonstrated escalating in tandem with the increase of hole concentration, as illustrated in Fig. 5b. These findings align with the Zener model of ferromagnetism proposed by Dietl *et al.*<sup>51</sup>, which posits that  $T_C$  is proportional to  $p^{1/3}$ , in which  $p$  represents the hole concentration.

To achieve effective FM ordering in semiconductor body, a minimum Mn content of approximately 2% is required to ensure a sufficiently high density of holes. However, the incorporation of a significant fraction of Mn atoms into GaAs films poses a formidable challenge because of the limited equilibrium solubility of transition metals in III-Vs, typically amounting to only a fraction of a percent. Therefore,  $\text{Ga}_{1-x}\text{Mn}_x\text{As}$  must be fabricated via a robust nonequilibrium process. Molecular beam epitaxy is commonly used to fabricate  $\text{Ga}_{1-x}\text{Mn}_x\text{As}$  films at relatively low temperatures ( $T_{\text{substrate}} \approx 250$  °C)<sup>50</sup>. An alternative approach involved the use of ion implantation followed by nanosecond pulsed laser annealing to grow FM  $\text{Ga}_{1-x}\text{Mn}_x\text{As}$  films<sup>54,55</sup>. Regrettably, defects such as Mn interstitials and anti-sites act as double donors, thereby offsetting a notable portion of the free holes in  $\text{Ga}_{1-x}\text{Mn}_x\text{As}$ <sup>56,57</sup>. In the meantime, Mn interstitials have the capability to form antiferromagnetic coupling with substitutional Mn, resulting in a reduction of the FM moment and a decrease in the  $T_C$ .

To elevate  $T_C$ , it is crucial to inhibit the formation of Mn interstitial defects and increase the hole concentration. Numerous studies have shown that optimizing the growth and annealing conditions, as well as introducing a capping semiconductor layer, effectively elevate  $T_C$ <sup>58–63</sup>. A comprehensive investigation, combining experimental and theoretical approaches, has demonstrated that the out-diffusion of Mn interstitials in  $\text{Ga}_{1-x}\text{Mn}_x\text{As}$  films can significantly augment the hole carrier density and  $T_C$ . In recent, the highest reported  $T_C$  for p-type  $\text{Ga}_{1-x}\text{Mn}_x\text{As}$  has reached 190 K with Mn content of around 10%<sup>60</sup>.

The level of spin polarization plays a pivotal role in the majority of spintronic functionalities. The attainment of high spin polarization occurs in a magnetic semiconductor when the Zeeman splitting of the conduction or valence band surpasses the Fermi energy<sup>16</sup>. Nevertheless, the magnitude and reliance of the Zeeman splitting on the orientation of the wavevector in magnetization exhibit distinct variations. Consequently, the expected polarization alters dramatically with the angle between the magnetization and current directions as well as the carrier concentration<sup>64</sup>. In theoretical calculations by Ogawa *et al.*, the carrier spin polarization of  $\text{Ga}_{1-x}\text{Mn}_x\text{As}$  is determined as 100% when  $x$  is greater than or equal to 0.125<sup>65</sup>. Through the utilization of Andreev reflection spectroscopy, a direct measurement of

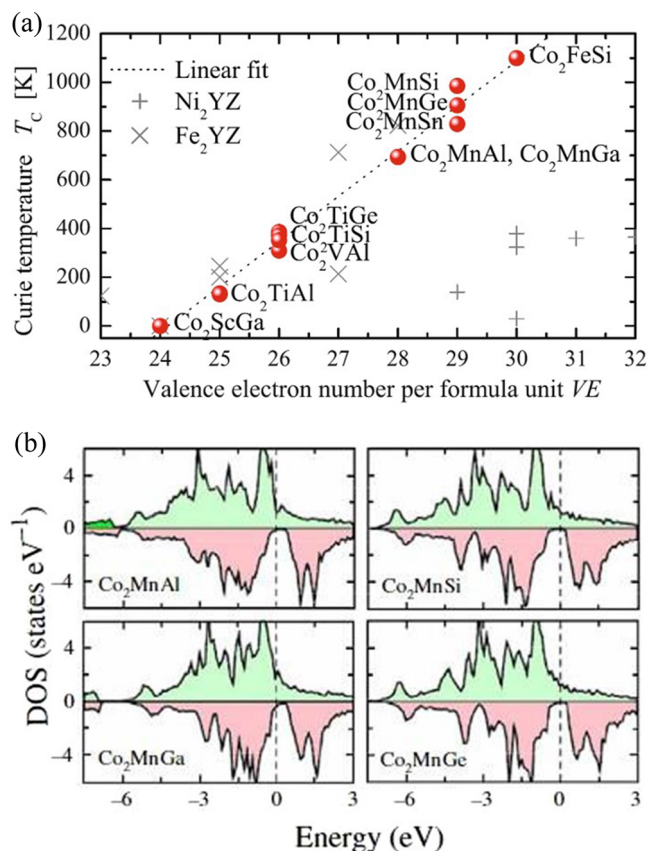


**Fig. 4 | The  $T_C$  and spin-projected DOS of  $\text{Co}_2$ -based Heusler compounds.** **a** The  $T_C$  of  $\text{Co}_2$ -based Heusler compounds shows a linear dependence on the number of valence electrons, and therefore, also on the magnetic moment. **b** Calculated spin-projected DOS for the  $\text{Co}_2\text{MnZ}$  compounds, where Z represents Al, Ga, Si, and Ge. It was observed that all of these compounds exhibit a finite spin-down DOS around the Fermi level. The figure a is reprinted with permission from ref. 37 Copyright 2013 by Springer Science+Business Media Dordrecht. The figure b is reprinted with permission from ref. 39 Copyright 2002 by the American Physical Society.

**Fig. 5 | The crystalline structure and  $T_C$  dependent carrier density for  $\text{Ga}_{1-x}\text{Mn}_x\text{As}$ .** **a** The unit cell of  $\text{Ga}_{1-x}\text{Mn}_x\text{As}$  with defects including  $\text{As}_{\text{Ga}}$  which is the As anti-site and  $\text{Mn}_i$  representing the Mn interstitial. **b** Experimentally obtained  $T_C$  is plotted as a function of hole density in a series of consistently annealed  $\text{Ga}_{1-x}\text{Mn}_x\text{As}$  samples. The carrier densities are determined through Raman scattering measurements, while the  $T_C$  is obtained from SQUID magnetometry. The samples exhibit a wide range of Mn content ( $0.02 < x < 0.085$ ) and also demonstrate variation in thickness ranging from 300 nm to 1200 nm. The figure (b) is reprinted with permission from ref. 52 Copyright 2005 by the Springer Nature.

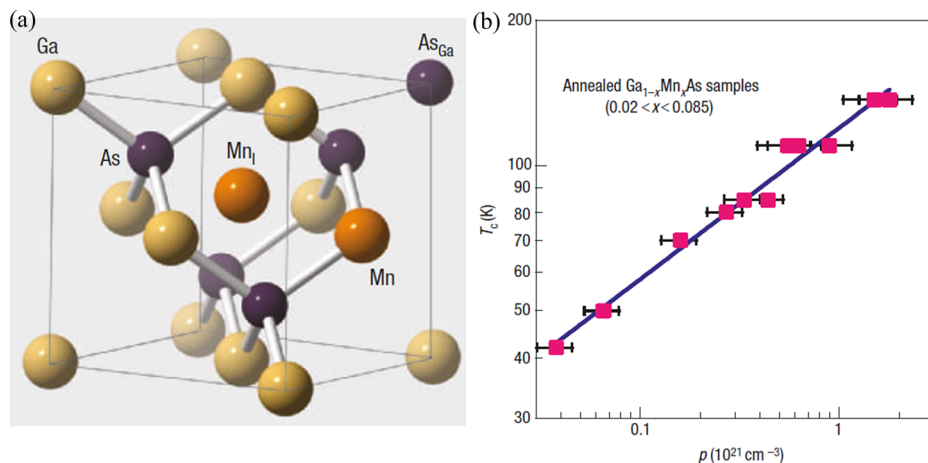
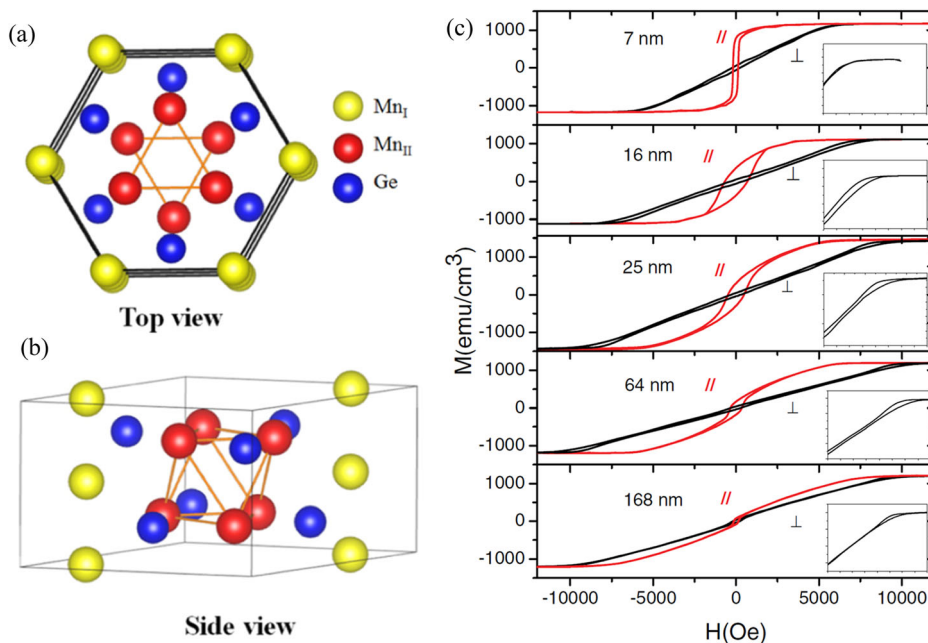


**Fig. 6 | The crystalline structure and Magnetic hysteresis curves of  $\text{Mn}_5\text{Ge}_3$ .** **a** The top view (left up) and **(b)**, side view (left down) of the crystal structure for  $\text{Mn}_5\text{Ge}_3$ . Colored spheres denote  $\text{Mn}_I$  (yellow),  $\text{Mn}_{II}$  (red), and Ge (blue). **c** Magnetic hysteresis curves were obtained by applying an external magnetic field in-plane and out-of-plane to  $\text{Mn}_5\text{Ge}_3$  films of varying thickness. Insets zoom into the positive field branches (ranging from 4000 to 12,000 Oe) in a perpendicular configuration. All measurements were conducted at 15 K. Figures **(a, b)** are reprinted with permission from ref. <sup>77</sup> Copyright 2018 by the American Physical Society. The **(c)** is reprinted with permission from ref. <sup>80</sup> Copyright 2012 by the American Physical Society.



polarization reveals a polarization of  $\geq 85\%$  in  $\text{Ga}_{1-x}\text{Mn}_x\text{As}$  ( $x = 0.05$ )<sup>66,67</sup>. Furthermore, it can serve as an epitaxially integrated emitter for the purpose of injecting spin-polarized carriers into nonmagnetic structures. The implementation of electrical spin injection from  $\text{Ga}_{1-x}\text{Mn}_x\text{As}$  into non-magnetic GaAs has been successfully achieved within a device structure, that is integrated with a GaAs-based nonmagnetic light-emitting diode (LED) used as a detector of spin-polarized holes<sup>68,69</sup>. However, despite the considerable efforts dedicated to  $\text{Ga}_{1-x}\text{Mn}_x\text{As}$ , the maximum  $T_C$  still remains far below RT<sup>64</sup>. Until now, the realization of semiconductors based spintronic devices operating at RT has remained elusive.

### Si- or Ge-based intermetallic compounds

The advancement of spintronics, a burgeoning field, relies on the studies on spin injectors with materials having high  $T_C$ , high spin polarization, as well as good compatibility with Si-based CMOS technology. As previously discussed, the ultra-low solubility of Mn in the semiconducting host presents a significant challenge in fabricating homogeneous films of dilute magnetic semiconductor with  $T_C$  above RT. The half-metallic Heusler alloys are the optimal candidate due to the desired high  $T_C$ . But, the intermixing with the substrate and/or lattice mismatch between Heusler alloy films and semiconductor substrate lead to significant reductions in spin polarization. Thus, when considering both high  $T_C$  and considerable spin polarization as well as the compatibility with CMOS technology, Si- or Ge-based transition metal alloys, such as  $\text{Fe}_3\text{Si}$ ,  $\text{Fe}_{1.7}\text{Ge}$ ,  $\text{Mn}_5\text{Ge}_3$ <sup>25–28,70</sup>, which can be directly grown on Si or Ge substrates with high quality interface attracted the researchers' attention for spintronic application. Here, the physical properties of the representative intermetallic compound  $\text{Mn}_5\text{Ge}_3$  will be given in this chapter.

$\text{Mn}_5\text{Ge}_3$  possesses a hexagonal crystal structure of  $D8_8$  type (space group  $P6_3/mcm$ ), as illustrated in Fig. 6. The lattice parameters of the relaxed  $\text{Mn}_5\text{Ge}_3$  unit cell at RT were experimentally determined to be:  $a = 7.184 \text{ \AA}$  and  $c = 5.053 \text{ \AA}$ <sup>71</sup>. The Mn atoms are situated in two distinct crystallographic sites.  $\text{Mn}_I$  occupies the position 4 d with 32 symmetry while  $\text{Mn}_{II}$  locates at position 6 g with  $mm$  symmetry. The atomic positions are delineated in the rectangular coordinates as follows<sup>72</sup>:

$\text{Mn}_I$  in (4 d) site:  $\pm(1/3, 2/3, 0; 2/3, 1/3, 1/2)$ ,

$\text{Mn}_{II}$  in (6 g) site:  $\pm(x, 0, 1/4; 0, x, 1/4; -x, -x, 1/4)$  with  $x = 0.2397$ ,

Ge in (6 g) site:  $\pm(x, 0, 1/4; 0, x, 1/4; -x, -x, 1/4)$  with  $x = 0.6030$ ,

The unit cell of  $\text{Mn}_5\text{Ge}_3$  comprise two periodic atomic layers stacked along the  $c$  axis. The planes at  $z = 0$  and  $z = 1/2$  exclusively consist of only  $\text{Mn}_I$  atoms which form a 2D hexagonal lattice, whereas the planes at  $z = 1/4$

and  $z = 3/4$  contain equal amounts of  $\text{Mn}_{II}$  and Ge atoms. In principle, there are two possible surface terminations for the  $\text{Mn}_5\text{Ge}_3$  epitaxial layer, either a Mn termination or a mixed Mn/Ge termination<sup>73</sup>.

In 1963, it was unveiled that  $\text{Mn}_I$  at position 4 d and  $\text{Mn}_{II}$  at position 6 g exhibit distinct magnetic moments,  $(3 \pm 0.1)$  and  $(2 \pm 0.1)$  Bohr magnetons respectively, via neutron powder diffraction patterns<sup>74</sup>. However, the polarized neutron diffraction measurements conducted at 77 K in 1964 revealed that  $\text{Mn}_I$  atoms have a smaller magnetic moment of  $1.7(1)\mu_B$  compared to  $\text{Mn}_{II}$  atoms with  $2.7(1)\mu_B$ <sup>75</sup>. Subsequent studies have experimentally demonstrated that the  $\text{Mn}_{II}$  atom carries a larger magnetic moment of  $3.23(2)\mu_B$  in comparison to the  $\text{Mn}_I$  atom ( $1.96(3)\mu_B$ )<sup>71,76</sup>. The smaller magnetic moment of  $\text{Mn}_I$  can be attributed to distinct coordination of Mn and the presence of direct Mn-Mn interactions over a relatively short distance. The moments of Mn atoms in the bulk  $\text{Mn}_5\text{Ge}_3$  are all aligned ferromagnetically along the hexagonal  $c$  axis, resulting in uniaxial anisotropy along the  $c$  axis<sup>71,77</sup>. The  $T_C$  of bulk  $\text{Mn}_5\text{Ge}_3$  closely approaches RT (296 K), and its saturation magnetization is  $2.60(2) \mu_B/\text{Mn}$  atom at 4.2 K.

Numerous studies have been conducted on the epitaxial growth of  $\text{Mn}_5\text{Ge}_3$  films on Ge substrates due to their potential application in spintronics. The epitaxial growth  $\text{Mn}_5\text{Ge}_3$  was initially achieved by matching the hexagonal (001) basal plane with the (111) plane of the Ge substrate<sup>28,78,79</sup>.  $\text{Mn}_5\text{Ge}_3$  films demonstrate robust ferromagnetism maintaining up to a temperature of  $T_C = 296 \pm 10 \text{ K}$ . When the  $\text{Mn}_5\text{Ge}_3$  film thickness is less than 20 nm, the easy magnetization axis aligns with the hexagonal basal plane, parallel to the interface between  $\text{Mn}_5\text{Ge}_3$  and Ge. As the film thickness exceeds 20 nm, there is a gradual reorientation of the easy magnetization axis away from the hexagonal (001) plane of  $\text{Mn}_5\text{Ge}_3$ , aligning instead parallel to the  $c$ -axis (perpendicular to the sample surface) (Fig. 6c)<sup>70,80</sup>. The findings are substantiated by theoretical computations grounded in Kittel's model which delineates the magnetic behavior of domains in uniaxial thin films. Further analyses suggest that for thicknesses below 10 nm, the magnetization is oriented in-plane with a monodomain-type structure dominated by magnetostatic anisotropy ( $4\pi M_s^2$  in which  $M_s$  is saturation magnetization). The  $\text{Mn}_5\text{Ge}_3$  layers display a distinct magnetic structure beyond 20 nm, characterized by a stripe-domain pattern attributed to the robust perpendicular uniaxial magnetocrystalline anisotropy<sup>80</sup>. In ferromagnetic resonance (FMR) experiments, the presence of a stripe domain was evidenced by the emergence of an acoustic FMR mode with a clearly defined resonance field<sup>81</sup>. Interestingly, this critical thickness is



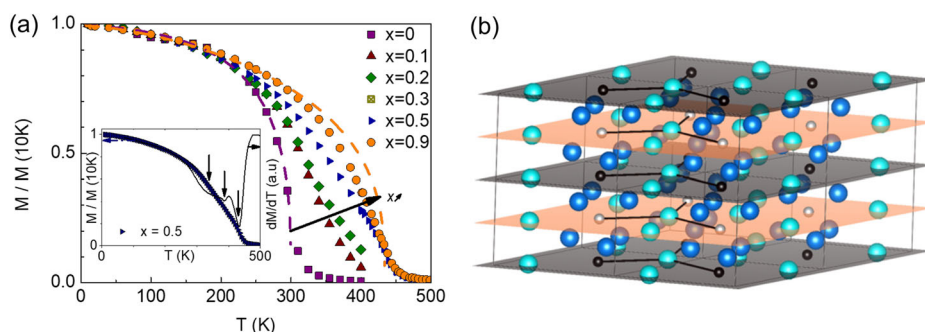


**Fig. 7 | The magnetization curves and atomic lattice of C-doped  $\text{Mn}_5\text{Ge}_3$ .**

**a** Magnetization as function of temperature for C-doped  $\text{Mn}_5\text{Ge}_3$  thin films with various carbon concentrations. The magnetic field of 1 Tesla was applied in plane. Temperature dependence of the magnetization (triangles) and its derivative (line) for the  $\text{Mn}_5\text{Ge}_3\text{C}_{0.5}$  film is depicted in the inset. The vertical arrows denote the various local minima corresponding to different  $T_C$  for  $x = 0.5$ . The figure is reprinted with permission from ref. 86 Copyright 2022 by the American Physical

Society. **b** Schematic representation of a hypothetical carbon superstructure in the  $\text{Mn}_5\text{Ge}_3\text{C}_{0.5}$  lattice. Colored spheres represent different entities, C (black),  $\text{Mn}_I$  (green),  $\text{Mn}_{II}$  (blue), and empty  $2(b)$  sites (light gray). Two distinct types of the  $\text{Mn}_I$  planes can be identified: one in gray where all  $2(b)$  voids are filled with carbon, and another in pink where all  $2(b)$  voids remain unoccupied. The figure is reprinted with permission from ref. 90 Copyright 2022 by the American Physical Society.

significantly lower compared to other materials with similar magnetic behavior. For example, it is approximately 50 nm in a Co film.

The  $T_C$  of intrinsic  $\text{Mn}_5\text{Ge}_3$  is limited to  $296 \pm 10$  K. From a practical perspective, it is preferable for spin injectors to possess a magnetic order well surpassing RT. Hence, diverse approaches are employed to boost  $T_C$ , such as, Fe, Sb or C co-doping<sup>82–84</sup>. By substituting one Mn atom with Fe,  $T_C$  was elevated to 319 K in  $\text{FeMn}_4\text{Ge}_3$ . Simultaneously, there is a notable increase in spin polarization from 42% in  $\text{Mn}_5\text{Ge}_3$  to approximately 60% in  $\text{FeMn}_4\text{Ge}_3$ <sup>82</sup>. Similarly, it has been demonstrated that the  $T_C$  of  $\text{Mn}_5\text{Ge}_3$  can be elevated by 14 K through the substitution of Sb for Ge, owing to the heightened magnetic coupling between Mn-3d and Sb-5p<sup>85</sup>.

One common method for improving the  $T_C$  in  $\text{Mn}_5\text{Ge}_3$  is through carbon doping. This pioneering work of Suergers *et al.* introduced that the incorporation of carbon into  $\text{Mn}_5\text{Ge}_3$  compounds leads to a significant enhancement of  $T_C$ <sup>18</sup>. In particular, the textured  $\text{Mn}_5\text{Ge}_3\text{C}_x$  films with  $x = 0.5$  demonstrate a significantly increased  $T_C$  of 435 K in comparison to bulk un-doped  $\text{Mn}_5\text{Ge}_3$  which exhibits a  $T_C$  of 296 K (see Fig. 7a)<sup>86–88</sup>. After C doping, there is a discernible reduction in the average magnetic moment of the Mn atom from  $2.6\mu_B$  to  $1\mu_B$ . A theoretical simulation conducted by Pochet *et al.* has elucidated that the heightened  $T_C$  of  $\text{Mn}_5\text{Ge}_3$  through carbon doping can be primarily attributed to the emergence of the 90° FM super-exchange between Mn atoms mediated by carbon. On the contrary, the reduction of interatomic distances between Mn atoms, stemming from the robust the strong hybridization between Mn 3d and C 2p orbitals, is deemed as a secondary effect<sup>89</sup>. Further investigation into the impact of carbon doping on  $\text{Mn}_5\text{Ge}_3$  was conducted by Spiesser *et al.* via utilizing scanning transmission electronic microscopy or<sup>55</sup> Mn nuclear magnetic resonance spectra<sup>86–88,90</sup>. It has been discovered that carbon enters interstitially in close to the 6(g) crystallographic positions, thereby occupying the 2(b) octahedral voids (Fig. 7b). The magnetic properties of the Mn atoms situated at the corners of a host octahedron are significantly altered by the presence of carbon. Consequently, both the magnetic moment and the magnetocrystalline anisotropy were reduced compared to the pristine  $\text{Mn}_5\text{Ge}_3$ .

As potential candidates for spin-injection, the electronic properties of  $\text{Mn}_5\text{Ge}_3$  were initially investigated theoretically by Picozzi *et al.* in 2004. As illustrated in Fig. 8, the full-potential linearized augmented plane-wave computation reveals the pronounced metallic character of  $\text{Mn}_5\text{Ge}_3$ , which is predominantly governed by Mn 3d contribution from the Fermi level up to a binding energy of 3.5 eV<sup>72</sup>. The spin polarization is determined to be 41% based on the band structure calculations. Soon afterwards, the theoretically predicted band structure was also empirically validated<sup>91–93</sup>. Subsequently, a variety of studies employing different techniques were conducted to assess the polarization values of  $\text{Mn}_5\text{Ge}_3$  layers. Point contact Andreev reflection measurements on  $\text{Mn}_5\text{Ge}_3$  epilayers have revealed a remarkable spin-

polarization of  $42 \pm 5\%$ <sup>27</sup>. Spin-resolved photoelectron spectroscopy measurements on  $\text{Mn}_5\text{Ge}_3$  (001)/Ge (111) films using photons with an energy of  $h\nu = 21.2$  eV have unveiled spin polarization of  $15 \pm 5\%$  at Fermi energy<sup>94</sup>. It has been discovered that the spin polarization of  $\text{Mn}_5\text{Ge}_3$  exhibits robust crystallographic anisotropy and heavily depends on the matrix element<sup>95</sup>. Hence, disparities in spin polarization have been observed across various experiments.

Due to the immense potential of  $\text{Mn}_5\text{Ge}_3$  in spintronics, it is essential to study the epitaxial growth of  $\text{Mn}_5\text{Ge}_3$  films on Ge substrates. In the initial stages, the majority of investigations were directed towards the growth of  $\text{Mn}_5\text{Ge}_3$  on Ge (111), wherein the solid phase epitaxy (SPE) method was employed to preclude the co-existence of secondary phases<sup>96–98</sup>. The SPE growth of  $\text{Mn}_5\text{Ge}_3$  films begins with the deposition of Mn films onto the Ge (111) substrates at RT, followed by thermal annealing at  $\sim 450^\circ\text{C}$  for several minutes to stimulate the inter-diffusion and phase nucleation<sup>28,79,98</sup>. Epitaxial  $\text{Mn}_5\text{Ge}_3$  films have been successfully fabricated, featuring a hexagonal basal plane (001) that aligns parallel to the (111) surface plane of Ge. The atomically abrupt interface was obtained, with virtually no threading dislocations being detectable.

Although extensive researches have been dedicated to investigating the epitaxial growth of  $\text{Mn}_5\text{Ge}_3$  layer on the Ge (111) substrate, it is also crucial to achieve the epitaxial growth of  $\text{Mn}_5\text{Ge}_3$  layer on the Ge (001), as it is practically compatible with the Si-based CMOS technology. The initial endeavor to cultivate  $\text{Mn}_5\text{Ge}_3$  on the Ge (001) substrates utilizing the SPE method was conducted at a substrate temperature of  $650^\circ\text{C}$ . Under such conditions, the  $\text{Mn}_5\text{Ge}_3$  film manifests itself in the form of a nano-island with  $(001)_{\text{Mn}_5\text{Ge}_3} \parallel (001)_{\text{Ge}}$ <sup>99,100</sup>. To effectively enhance the quality of the  $\text{Mn}_5\text{Ge}_3$  film on Ge (001), non-equilibrium ultrafast solid phase epitaxy (ultrafast-SPE) is employed. In this process, ultrafast annealing is utilized to modify the kinetics and thermodynamics during the growth of  $\text{Mn}_5\text{Ge}_3$ . Consequently, epitaxial  $\text{Mn}_5\text{Ge}_3$  films were successfully grown on Ge (001) with the in-plane axis [001] of  $\text{Mn}_5\text{Ge}_3$  (100) plane parallel to the [110] axis of the Ge (001) substrate<sup>101–103</sup>.

Numerous studies have been dedicated to the development of spin transport devices based on  $\text{Mn}_5\text{Ge}_3$ . As reported, the observation of spin accumulation and precession up to 10 K was documented in  $\text{Mn}_5\text{Ge}_3\text{C}_{0.8}/\text{Al}_2\text{O}_3/\text{n}^+-\text{Ge}$  ( $10^{20}\text{ cm}^{-3}$ ) tunneling contacts through the adoption of three-terminal (3-T) Hanle-effect measurements<sup>104</sup>. The lifetime of spin at  $T = 4$  K is extracted to be 38 ps and the spin diffusion length is calculated to be approximately 367 nm. However, such a spin signal could potentially be generated by localized states within the tunnel contact through two-step tunneling or impurity-assisted tunneling magnetoresistance. To eliminate such possibilities, investigation into the direct Schottky tunnel contact between  $\text{Mn}_5\text{Ge}_3$  and As-doped-Ge (111) ( $10^{18}\text{ cm}^{-3}$ ) was conducted<sup>17</sup>. Utilizing 3 T geometry, which comprises one single FM contact that used as



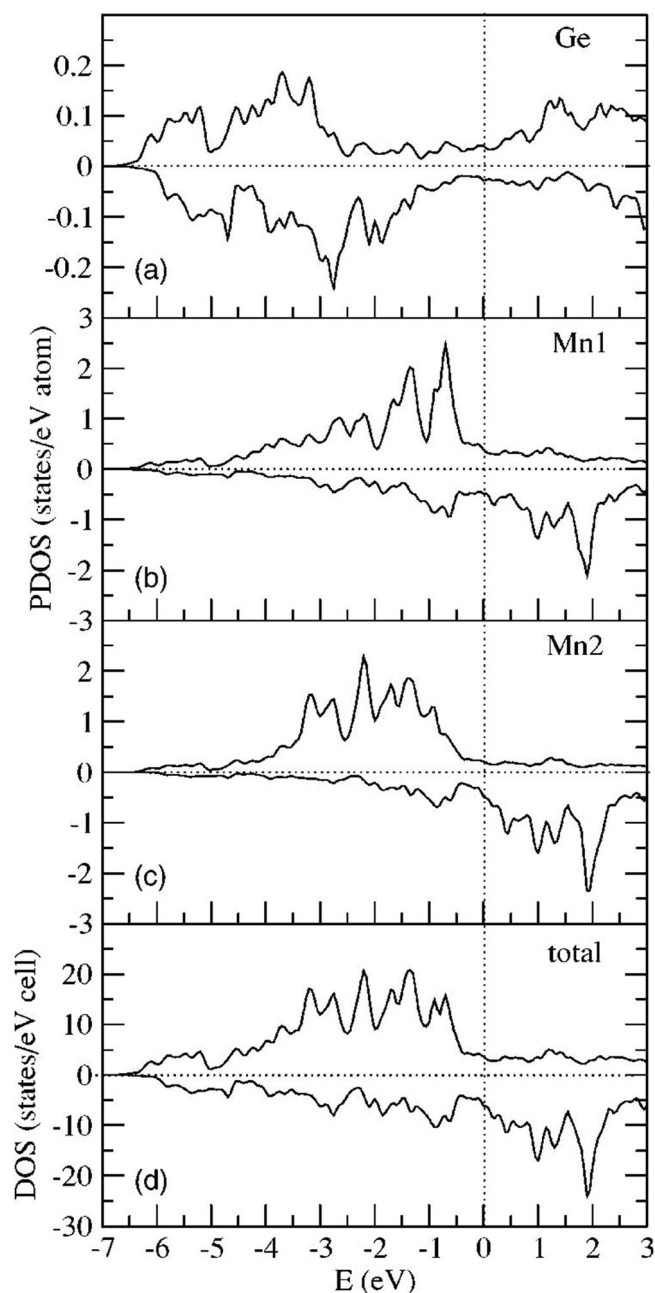


**Fig. 8 | The density of states of  $\text{Mn}_5\text{Ge}_3$ .** Partial density of states of (a), Ge, (b), Mn<sub>1</sub>, and (c), Mn<sub>2</sub>, and the total density of states is displayed in (d). Majority (minority) spin components are depicted along the positive (negative) y-axis. Fermi energy is defined as zero on the energy scale. The figure is reprinted with permission from ref. 72 Copyright 2004 by the American Physical Society.

the spin injector and detector, apparent Hanle and inverted Hanle signals with characteristic features of spin accumulation and spin precession were observed up to 200 K. However, the 3-T geometry is highly susceptible to spurious signals, such as Hall or anisotropic magnetoresistance effects, due to the presence of a nonzero charge current at the detector junction. Hence, further research on the non-local spin transport device based on  $\text{Mn}_5\text{Ge}_3$  films is imperative to propel the advancement of spintronics.

## 2D ferromagnetic materials

The emergence of 2D materials has attracted much attention due to their tremendous electrical, optical, and magnetic properties and their broad range of applications in spintronics<sup>105–108</sup>. The atoms in monolayer 2D

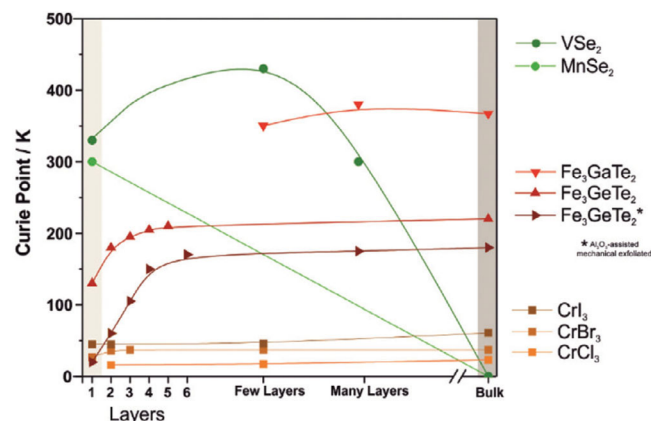


**Fig. 9 | Dependence of the Curie point on the layer number of recently discovered 2D ferromagnets.** Data has been sourced from literature as follows:  $\text{VSe}_2$ ,  $\text{MnSe}_2$ ,  $\text{Fe}_3\text{GaTe}_2$ ,  $\text{Fe}_3\text{GeTe}_2$ , (mechanically exfoliated, assisted by  $\text{SiO}_2/\text{Si}$  or  $\text{Al}_2\text{O}_3$ ), and  $\text{CrI}_3$ ,  $\text{CrBr}_3$ ,  $\text{CrCl}_3$ . The figure is reprinted with permission from ref. 115 Copyright 2024 by the Wiley-VCH GmbH.

materials are typically bound together by robust covalent bonds, while the individual layers are interconnected through the subtle and delicate vdWs interaction<sup>108</sup>. Consequently, the distinctive characteristics and adaptability of 2D magnetic materials have provided a captivating platform for the exploration of novel spintronic concepts with exceptional controllability. The initial attempts to isolate magnetic 2D materials were conducted towards the end of 2016, when researchers successfully exfoliated monolayer and few-layer  $\text{NiPS}_3$ <sup>109</sup>, and  $\text{FePS}_3$ <sup>110,111</sup>. The magnetic ordering of these compounds is preserved down to the monolayers limit which was illustrated by the Raman measurements. Then, further breakthrough was made in 2017, with the first experimental confirmation of ferromagnetism via magneto-optic Kerr microscopy in atomically thin  $\text{CrI}_3$ <sup>112</sup> and  $\text{CrGeTe}_3$ <sup>113</sup>, respectively.

To date, a great deal of 2D materials, which are often obtained through mechanical exfoliation, exhibit an intrinsic FM order<sup>112–114</sup>. Several studies demonstrate that the FM order and the  $T_C$  of 2D material depend upon the layer numbers and the thickness of a given material<sup>113</sup>. The correlation between the layer number and  $T_C$  of recently discovered 2D ferromagnets is illustrated in Fig. 9<sup>115</sup>. According to the dependence of  $T_C$  on the layer numbers, three distinct trends have been identified for three different categories of materials: i)  $\text{CrX}_3$  ( $X = \text{I, Br, Cl}$ ) – these materials usually exhibit a significantly low  $T_C$  (far below 100 K) at the 2D scale, which marginally increased in their bulk form<sup>116</sup>; ii) Fe-Ge-Te ternary compounds ( $\text{Fe}_3\text{GeTe}_2$ ,  $\text{Fe}_3\text{GaTe}_2$ ) – these materials usually exhibit a slight increase in the  $T_C$  in the multi-layer structures than the bulk and then a remarkable decrease when down to the monolayer limit<sup>114,117,118</sup>; iii)  $\text{MSe}_2$  ( $M = \text{Mn, V et. al}$ ) – they surprisingly demonstrate RT ferromagnetism in low dimensionality despite the fact that their bulk crystals do not exhibit FM, unlike most 2D ferromagnets, which derive their magnetic properties from bulk crystals<sup>119–121</sup>.

In addition to the aforementioned 2D ferromagnets, 2D anti-ferromagnetic material has also garnered significant attention recently due to their unique properties such as terahertz resonance and no stray fields, particularly suitable for spintronics. Typical representative is the  $\text{MPX}_3$  family ( $M = 3\text{d transition metals}$ ;  $X = \text{chalcogen atoms}$ ) which have similar crystal structures, and have been exfoliated into monolayers<sup>122,123</sup>. It's remarkable the magnetism of these materials exhibits significant variation depending on the transition metal atom  $M$ . For instance, Mn-based compounds exhibit a Néel AFM order where the spin states in the nearest neighbor metal atoms have an opposite orientation, while Fe-, Co-, and Ni-based compounds display a zig-zag AFM order where the spin-state of the adjacent metal atom chains along the zigzag direction has an opposite orientation<sup>123</sup>. Magnetic measurements demonstrated that the Néel

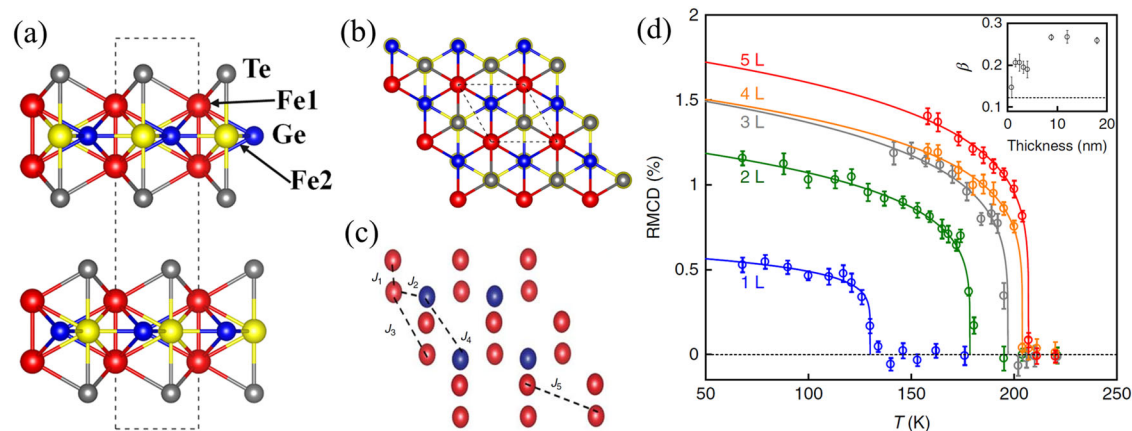


**Fig. 10 | The atomic lattice, exchange coupling and RMCD signal of  $\text{Fe}_3\text{GeTe}_2$ .** The atomic lattice of bulk  $\text{Fe}_3\text{GeTe}_2$  is depicted in Side view (a) and middle top views (b) showcasing its crystal unit cell marked by dashed rectangular and rhombic shapes<sup>126</sup>. c The schematic diagram illustrates the exchange coupling in  $\text{Fe}_3\text{GeTe}_2$ <sup>108</sup>. d Remanent RMCD signal is plotted as a function of temperature across a series of selected few-layer flakes (1 L, monolayer; 2 L, bilayer; 3 L, trilayer; 4 L, four layers;

5 L, five layer); The derived values of the exponent  $\beta$  are depicted as a function of thickness in the inset, revealing a dimensional transition from 3D to 2D Ising ferromagnetism<sup>117</sup>. The figure a and b are reprinted with permission from ref. 126 Copyright 2019 by the American Chemical Society. The figure c is reprinted with permission from ref. 108 Copyright 2021 AIP Publishing LLC. The figure d is reprinted with permission from ref. 117 Copyright 2018 by the Springer Nature.

transition temperature  $T_N$  ranges from 82 to 155 K in bulk Ni, Fe, Mn, and Co based  $\text{MPSe}_3$  or  $\text{MPSe}_3$ <sup>122</sup>. Additionally, the magnetic anisotropy energy of this family materials is also significantly different. For instance,  $\text{FePSe}_3$  demonstrates a significantly larger magnetic anisotropy energy attributed to its strong Ising-like anisotropy, while  $\text{MnPSe}_3$  shows smaller magnetic anisotropy energy attributed to a pronounced XY anisotropy<sup>124,125</sup>.

One of the most studied 2D magnetic material is  $\text{Fe}_3\text{GeTe}_2$  (FGT). FGT possesses a layered hexagonal crystal structure, consisting of  $\text{Fe}_3\text{Ge}$  slabs partitioned by the vdW bonded Te layers. The crystal structure of bulk FGT is depicted in Fig. 10a–b<sup>126</sup>. The Fe atoms within the unit cell are situated in two inequivalent Wyckoff sites, identified as Fe<sub>1</sub> and Fe<sub>2</sub> in Fig. 10a. The magnetic moment of Fe<sub>1</sub><sup>3+</sup> is about  $1.7 \mu_B$  and that of Fe<sub>2</sub><sup>2+</sup> is about  $1 \mu_B$ . As depicted in Fig. 10c, the magnetic coupling parameters governing interlayer Fe<sub>1</sub>–Fe<sub>2</sub> coupling and Fe<sub>1</sub>–Fe<sub>1</sub> coupling are 20.41 meV and 23.48 meV, respectively, which collectively control the ferromagnetism of FGT. It means the coupling between perpendicular Fe atoms dominates the ferromagnetism in FGT. However, the coupling between Fe and Te atoms also makes contribution to the ferromagnetism. In principle, the distance between adjacent FGT layers hold a pivotal role in tuning the magnetic interactions. Kim and Hu et al. have discovered that the magnetic interaction between adjacent layers of FGT is regulated by the indirect interaction between oxygen *p* orbitals where oxygen atoms originate from an oxide layer (O-FGT) naturally formed on top of exfoliated FGT<sup>127,128</sup>.

The pioneering study of the inherent ferromagnetism in single-layer FGT was conducted by Zhuang et al. in 2016<sup>129</sup>. In their work, density functional theory (DFT) calculations revealed the ease of mechanically exfoliating nanosheets from the bulk phase. The band structure around the Fermi level is predominantly influenced by Fe 3 *d* orbitals, which leads to the fulfillment of the Stoner criterion and, consequently, itinerant ferromagnetism. In 2018, Fei et al. successfully exfoliated FGT bulk crystals into monolayer onto a gold film which is evaporated on top of  $\text{SiO}_2/\text{Si}$ <sup>117</sup>. The  $T_C$  of monolayer FGT was revealed to be 130 K by X-Ray Magnetic Circular Dichroism (RMCD) measurement. In addition, layer-number-dependent investigations have unveiled a transition from 3D to 2D itinerant ferromagnetism when the thicknesses are decreased to thinner than 4 nm (equivalent to five layers) (Fig. 10d, inset). Subsequently, Deng et al. employed the  $\text{Al}_2\text{O}_3$ -assisted exfoliation method instead of conventional mechanical exfoliation with the aim of protecting the intralayer bonding<sup>114</sup>. The  $T_C$  of monolayer FGT was determined to be 68 K and 30 K through RMCD and remanent anomalous Hall resistance measurement, respectively, which were significantly lower than the one reported by Fei et al.<sup>114,117</sup>. Moreover, the itinerant ferromagnetism with an

out-of-plane magnetocrystalline anisotropy persists down to monolayer in FGT. However, Min et al. have recently highlighted that the FGT's ferromagnetism cannot be explained solely by the itinerant picture. Instead, it is suggested to exist in an intermediate regime with both the itinerant and the localized spin states, as derived from the electronic structure calculations<sup>130</sup>. Therefore, the investigation of FGT still needs further demonstration to clarify the controversy about the origin of magnetism and the disparity in the  $T_C$ .

As reported, the  $T_C$  of FGT depends on many factors, such as the layers number, the fabrication environment and 3 d element doping. FM metallic FGT exhibits a  $T_C$  near 220 K in its bulk state<sup>131</sup>. The reported  $T_C$  exhibited dramatic decreases with the reduced number of layers in FGT when the thickness is less than 25 nm. Layer-number-dependent investigations have revealed a rapid decrease in the  $T_C$  from 207 K for five layers to 130 K for the monolayer via RMCD measurement and Anomalous Hall effect measurements<sup>117,132</sup>. Moreover, the variation in the probed  $T_C$  may stem from diverse synthesis environments of FGT<sup>133,134</sup>. Zhang et al. deposited FGT flakes onto three distinct substrates, namely Al, Au, and  $\text{SiO}_2$ . The substitution of substrate from Al to Au could significantly improve  $T_C$  value from 105 to 180 K for 10 nm-FGT film. Such evident modulation of  $T_C$  by substrates may be ascribed to the distortion of lattice and the redistribution of charge between the FGT sample and the substrate<sup>133</sup>. Meanwhile, Deng et al. managed to boost  $T_C$  of the monolayer FGT to RT via an ionic gate, much higher than that of the bulk<sup>114</sup>. Finally, doping with transition-metal atoms is an effective method to tune the magnetic properties of FGT. It was demonstrated the  $T_C$  can be improved to 320 K in  $\text{Fe}_{3+1.80}\text{GeTe}_2$  layer after the adoption of Fe atoms during the MBE growth<sup>135,136</sup>. However, the influence of Co dopant in FGT is complicated. Both the  $T_C$  and moment of FGT are gradually suppressed upon Co doping while a certain amount of Co dopant in  $\text{Fe}_3\text{GeTe}_2$  would improve the  $T_C$  to 325 K<sup>137,138</sup>.

The electronic properties of 2D FGT were newly investigated by Jung et al.<sup>130</sup>. It has been contended that the FGT's ferromagnetism cannot be simply explained using the itinerant picture. Rather, it is posited to exist in an intermediate regime with both the itinerant and the localized spin states. FGT demonstrates a robust energy-dependent spin polarization (Fig. 11) arising from the simultaneous presence of itinerant and localized spin states<sup>130</sup>. The spin polarization dependent on energy of a FM electrode has been effectively detected by observing the variation in the TMR value in the spin-valve device configuration of MTJs. The vertical tunneling SV device based FGT electrodes sandwiching wide-band h-BN,  $\text{WSe}_2$  or  $\text{MoS}_2$  as a NM tunnel barrier have been fabricated<sup>130,139</sup>. The observed magnetoresistance ratio (MR ratio) of 160% at 4.2 K for the intrinsic MTJ serves as a

compelling validation of the exceptional performance of the device. The spin polarization of 66% was extracted from the MR ratio, corresponding to 83% and 17% of the majority and minority carriers, respectively<sup>139</sup>. By manipulating the electrical bias, it is highly possible to modulate and even reverse the net spin polarization of the injected carriers. This phenomenon ultimately leads to changes in sign of the tunnelling magnetoresistance<sup>130</sup>. Through electrolyte gating, the tunneling MR ratio of FGT/h-BN/FGT MTJ

has been significantly improved by 2.5 times, from 26% to 65%, the spin polarization from 0.34 to 0.49<sup>140</sup>. Moreover, nonlocal SVs with FGT as the spin source and detector were fabricated and employing multilayer graphene as the spin transport channel. The efficiency of spin injection was approximated to be around 1%, close to conventional nonlocal SVs with transparent contacts between FM electrodes and the graphene channel<sup>141</sup>.

Although great progress has been made in the development of 2D ferromagnetism and related devices, it is still a great challenge to produce monolayered materials with i) RT FM order, ii) good air stability, and iii) repeatability on a large scale, which are prerequisite to achieve practical applications. Recent discoveries of monolayer  $\text{MnSe}_x$  (usually,  $x = 1$  or 2) and  $\text{VSe}_2$  exhibiting intrinsic ferromagnetism at RT, coupled with the controlled synthesis of pioneering materials  $\text{Cr}_7\text{Te}_8$  and  $\text{CrTe}_2$  along with its exceptional and air-stable FM characteristics, open novel avenues for exploration into 2D magnetism and their applications in spintronic device<sup>119,120,142,143</sup>. Therefore, we envision that the heterostructures of vdW materials with exceptional spin-related properties at RT will pave the way for the realization of all-vdW-material-based spintronic devices at RT in the future.

## Summary and outlook

In summary, we review various FM materials for highly efficient electrical spin injection across the ferromagnet/semiconductor interface, which is expected to become a mainstream technology in future microelectronics. The  $T_C$  and spin polarization of various FM/semiconductor materials are summarized in Table 1. (1) Heusler alloys possess the desired high  $T_C$  above RT and theoretically 100% spin polarization. Nevertheless, the absence of local ordering structure and intermixing between Heusler alloy films and semiconductor substrate pose a barrier to achieving half-metallic electron transport property at RT, as theoretically predicted in the bulk Heusler alloy. (2) Dilute magnetic semiconductors have comparable resistance with semiconductor channel, which could reduce the interface resistance and further promote the improvement of the spin injection. Nevertheless, a further increase of  $T_C$  has always been a major goal in dilute magnetic semiconductors. (3) The Si- or Ge-based intermetallic compounds offer several advantages including considerable spin polarization, the high-quality interface and compatibility with CMOS technology. In essence, the Si- or Ge-based transition metal alloys are deemed to be the most auspicious for application in spintronics. (4) 2D FM materials hold great appeal for spintronics owing to their infinitesimal thickness and exceptional physical properties. However, the air stability and reproducibility of 2D material with desirable performances is still full of challenges.

Although the advent of the aforementioned magnetic materials has certainly injected new vitality into the realm of spintronics, the building of spin-based devices operated at RT remains full of challenges. Herein, several strategies are proposed to overcome the main obstacles in applying such spintronics devices in nonvolatile logic-in-memory. First, there is a pressing need for intensive research to advance the development of atomically controlled Heusler films, which has been utilized as a spin source due to their

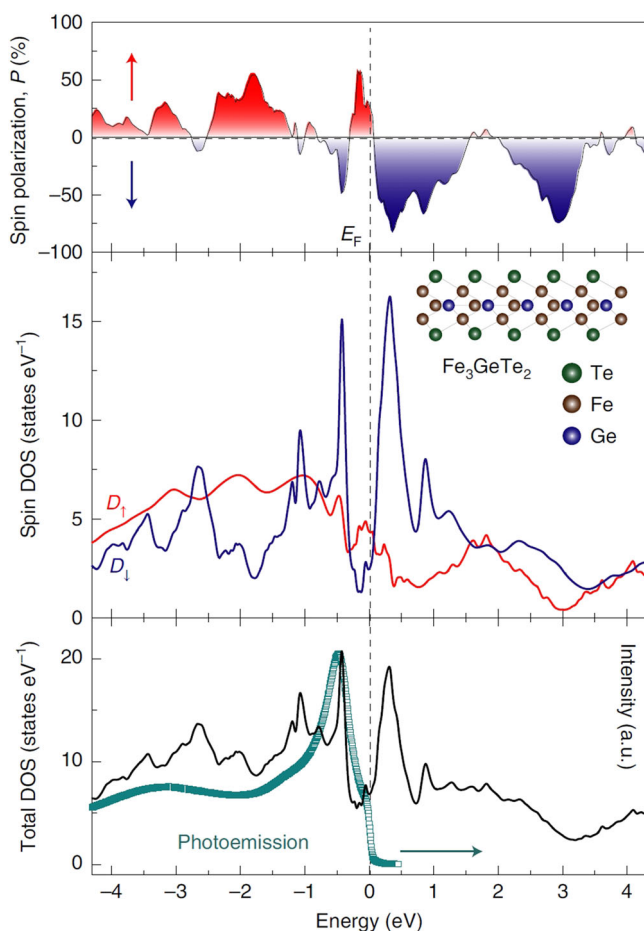


**Fig. 11 | The spin polarization and DOS of  $\text{Fe}_3\text{GeTe}_2$ .** The spin polarization ( $P$ ) dependent on the energy for  $\text{Fe}_3\text{GeTe}_2$  material (top panel) extracted from the 2D metallic ferromagnetism's spin-polarized DOS ( $D\uparrow$  and  $D\downarrow$ ) (depicted in the middle panel). The multilayered FGT's total DOS ( $D\uparrow + D\downarrow$ ) (depicted in the bottom panel) is derived from DFT +DMFT calculations. The open cyan squares visually represent momentum-averaged intensity of the photoemission spectroscopy measurements for the FGT. The figure is reprinted with permission from ref. 130 Copyright 2022 by the Springer Nature.

**Table 1 | Summary of the  $T_C$  and spin polarization in various FM/semiconductor materials**

| FM injector                               | Heterojunction structure                                    | $T_C$ (K)     | Spin polarization     | Characterization of $P$            | Main applications          | Refs.       |
|---|---|---------------|-----------------------|------------------------------------|----------------------------|-------------|
| CoMnSi                                    | CoMnSi/ $\text{Al}_2\text{O}_3$ /CoFeSi                     | ~985          | ~61% at 10 K          | Julliere's formula                 | MRAM                       | 45          |
| $\text{Co}_2\text{FeAl}_x\text{Si}_{1-x}$ | $\text{Co}_2\text{FeAl}_x\text{Si}_{1-x}$ /GaN              | $1100 \pm 20$ | ~20% at 300 K         | nonlocal Hanle Signal              | spin lasers                | 157         |
| $\text{Ga}_{1-x}\text{Mn}_x\text{As}$     | $\text{Ga}_{1-x}\text{Mn}_x\text{As}$ /GaAs                 | ~190          | ~80% at 4.6 K         | oblique Hanle effect technique     | light-emitting diode (LED) | 60,67       |
| $\text{Mn}_5\text{Ge}_3$                  | $\text{Mn}_5\text{Ge}_3$ /Ge                                | ~296          | $42 \pm 5\%$ at 1.2 K | Andreev reflection spectroscopy    | spin computing circuits    | 27,28       |
| $\text{Fe}_3\text{Si}$                    | $\text{Fe}_3\text{Si}$ /Si                                  | ~803          | 7-30% at 300 K        | Nonlocal lateral spin Valve signal | spin computing circuits    | 158         |
| $\text{Fe}_3\text{GeTe}_2$                | $\text{Fe}_3\text{GeTe}_2$ /hBN/ $\text{Fe}_3\text{GeTe}_2$ | $\leq 220$    | ~66% at 4.2 K         | Julliere's formula                 | MRAM                       | 114,117,139 |
| $\text{Fe}_5\text{GeTe}_2$                | $\text{Fe}_5\text{GeTe}_2$ /graphene                        | ~310          | 1.2-44.9% at 300 K    | Nonlocal lateral spin Valve signal | spin computing circuits    | 159         |
| Co  | Co/ $\text{TiO}_x$ /graphene                                | ~1400         | ~12.5% at 300 K       | Fert-Jaffres calculations          | spin computing circuits    | 30          |
| CoFe                                      | CoFe/MgO/Si   | ~1250         | ~43% at 300 K         | Nonlocal Hanle signal              | spin computing circuits    | 160         |



half-metallicity at RT. First principles calculations and materials informatics, based on available databases<sup>32,144</sup>, have been utilized to identify pertinent combinations of interfacial atomic bonding, crystalline orientation and surface termination which are aimed at maintaining the atomic ordering in the vicinity of their interface and surfaces. For example, the epitaxial growth of Co<sub>2</sub>MnSi on Si has been realized recently which paves the way for high-performance semiconductor spintronic devices<sup>145</sup>. In addition, the half-metallicity of Heusler films could enhance better operation ability in STT based devices owing to their intrinsically low Gilbert damping constants for fast magnetization reversal with low switching current density<sup>146</sup>. On the other side, a further increase in  $T_C$  of dilute magnetic semiconductor can be achieved by non-equilibrium doping in new material system, gate tunability, materials interfaces engineering or proximity effects at ferromagnet/semiconductor junctions, resulting in increased spin and hole densities, ideal for the development of advanced spintronic devices<sup>147,148</sup>. Recently, a consensus appears to have emerged in the pursuit of achieving  $T_C$  above RT via introducing magnetic dopants into vdW-layered semiconductors, such as Fe-doped MoS<sub>2</sub>, V-doped WSe<sub>2</sub>, or Cr-doped GaTe<sup>149</sup>.

Second, albeit investigations on the above-mentioned magnetic materials in thin films (tens nm) have been ongoing for many years, recent advancements in nanoscale characterization and device fabrication down to the 2D limit (several atomic layers) have created opportunities for exploring novel physical phenomena and developing cutting-edge spintronic devices. Currently, the exploration of integration engineering and the comprehension of the growth process of 2D ferromagnets are still in their nascent stages, despite some initial advancements being achieved. The future prospect for the advancement of spintronics may closely align with development in robust 2D magnetic materials with RT ferromagnetism. With the advent of large-scale growth of advanced 2D materials via chemical vapor deposition (CVD) methods, it is indubitable to anticipate a genuine potential in the new generation of 2D spintronics logic devices on large-scale. For example, the  $T_C$  of graphene-based magnetic materials was improved to exceeding RT ( $\geq 300$  K) with a saturation magnetization as high as  $4.1 \times 10^{-7}$  emu-mm<sup>-2</sup> by controlling CVD growth process<sup>150</sup>. In addition, the spin transport capabilities also can be improved by utilizing the 2D semiconductor channel, such as MoS<sub>2</sub>, black phosphorous or graphene, with the ferromagnetic tunnel contacts<sup>30,151,152</sup>. The higher spin diffusion length of  $\sim 13.6 \mu\text{m}$  was demonstrated in graphene spin devices on standard large-scale substrates<sup>30,31</sup>. The outstanding performance in 2D-based FM/semiconductor heterostructure can be attributed to the exclusive features of 2D crystal such as atomic-level thickness control, near-perfect crystallography without dangling bonds, and novel electronic structure-guided interfaces with tunable hybridization and proximity effects, which lead to an entirely new group of spinterfaces<sup>153</sup>. This new aspect has sparked significant interest, prompting both theoretical and experimental endeavors aimed at developing an entirely novel category of vdWs interfaces for efficient spin transmission and dynamic control through exotic heterostructures.

Third, numerous emerging spin-based effects in topological insulators or heavy metals, such as spin pumping via the (inverse) Rashba-Edelstein effect, which has been utilized for generating pure spin current in neighboring nonmagnetic layer through the magnetization precession in FM layer. And the (inverse) Rashba-Edelstein effect has been harnessed for injecting/detecting spin in Rashba interfaces or topological insulator heterostructures<sup>154</sup>. Topological insulator (Bi<sub>2</sub>Se<sub>3</sub>), characterized by spin-momentum-locked surface states arising from strong spin-orbit coupling (SOC), possesses the capability to impart spin current into neighboring materials across the interface through SOT<sup>155</sup>. Inversely, the injection of a spin current induces the corresponding spin polarization and charge current. Other types spin-charge conversion can also be achieved through SOC effects of 3D conductors, specifically the observation of the spin Hall effect in the heavy metals (such as Pt, Ta)<sup>156</sup>. Such spin-charge conversion phenomena described holds significant implications for the field of spintronics technologies, which center around the generation and detection of spin

currents. Therefore, it is highly feasible to achieve low-power and all-electric control of spintronic devices devoid of reliance on magnetic fields. These advancements are poised to expedite the progress of beyond-CMOS device application.

Spintronic devices, which harness the dual degrees of freedom of spin and charge in electrons, have the potential introducing new capabilities to the microelectronics industry. Nevertheless, in order to satisfy the ever-growing demands of chip level integration of magnetism and standard electronics in spintronics, innovation in terms of materials, processes and devices are still indispensable.

## Data availability

No datasets were generated or analysed during the current study.

Received: 31 July 2024; Accepted: 31 December 2024;

Published online: 28 March 2025

## References

1. Dieny, B. et al. Opportunities and challenges for spintronics in the microelectronics industry. *Nat. Electron.* **3**, 446–459 (2020).
2. Awschalom, D. D. & Flatté, M. E. Challenges for semiconductor spintronics. *Nat. Phys.* **3**, 153–159 (2007).
3. Žutić, I., Fabian, J. & Sarma, S. D. Spintronics: Fundamentals and applications. *Rev. Mod. Phys.* **76**, 323 (2004).
4. Tang, W., Liu, H., Li, Z., Pan, A. & Zeng, Y. Spin-orbit torque in van der waals-layered materials and heterostructures. *Adv. Sci.* **8**, 2100847 (2021).
5. Baibich, M. N. et al. Giant magnetoresistance of (001)Fe/(001)Cr magnetic superlattices. *Phys. Rev. Lett.* **61**, 2472 (1988).
6. Dieny, B. et al. Magnetotransport properties of magnetically soft spin-valve structures. *J. Appl. Phys.* **69**, 4774 (1991).
7. Moodera, J. S., Kinder, L. R., Wong, T. M. & Meservey, R. Large magnetoresistance at room temperature in ferromagnetic thin film tunnel junctions. *Phys. Rev. Lett.* **74**, 3273 (1995).
8. Ikeda, S. et al. Tunnel magnetoresistance of 604% at 300 K by suppression of Ta diffusion in CoFeB/MgO/CoFeB pseudo-spin-valves annealed at high temperature. *Appl. Phys. Lett.* **93**, 082508 (2008).
9. Kato, T., Iwata, S. & Oshima, D. Progress on efficient current-induced magnetization switching. *Electr. Eng. Jpn.* **212**, 3–10 (2020).
10. Garelo, K. et al. SOT-MRAM 300mm integration for low power and ultrafast embedded memories. In *2018 IEEE Symposium on VLSI Circuits*. 81–82 (2018).
11. Bhatti, S. et al. Spintronics based random access memory: a review. *Mater. Today* **20**, 530 (2017).
12. Min, B. C. Interface engineering of spin-tunnel contacts to silicon. Doctoral dissertation, University of Twente, Enschede, Netherlands (2007).
13. Johnson, M. & Silsbee, R. H. Interfacial charge-spin coupling: Injection and detection of spin magnetization in metals. *Phys. Rev. Lett.* **55**, 1790 (1985).
14. Schmidt, G., Ferrand, D., Molenkamp, L. W., Filip, A. T. & Van Wees, B. J. Fundamental obstacle for electrical spin injection from a ferromagnetic metal into a diffusive semiconductor. *Phys. Rev. B* **62**, R4790 (2000).
15. Kravchenko, V. Y. & Rashba, E. I. Spin injection into a ballistic semiconductor microstructure. *Phys. Rev. B* **67**, 121310 (2003).
16. Wolf, S. A. et al. Spintronics: a spin-based electronics vision for the future. *Science* **294**, 1488 (2001).
17. Spiesser, A., Saito, H., Jansen, R., Yuasa, S. & Ando, K. Large spin accumulation voltages in epitaxial Mn<sub>5</sub>Ge<sub>3</sub> contacts on Ge without an oxide tunnel barrier. *Phys. Rev. B* **90**, 205213 (2014).
18. Fischer, I. A., Sürgers, C., Petit, M., LeThanh, V. & Schulze, J. Mn<sub>5</sub>Ge<sub>3</sub>C<sub>0.8</sub> contacts for spin injection into Ge. *ECS Trans* **58**, 29 (2013).

19. Tang, J. & Wang, K. L. Electrical spin injection and transport in semiconductor nanowires: challenges, progress and perspectives. *Nanoscale* **7**, 4325 (2015).
20. Zhang, S. Y. et al. Bottom-Up synthesis of  $\text{Co}_x\text{Sn}_{1-x}\text{S}$  nanosheets: A ferromagnetic and photoconductive semiconductor. *Adv. Funct. Mater.* **33**, 2303847 (2023).
21. Tanaka, M. Recent progress in ferromagnetic semiconductors and spintronics devices. *Jpn. J. Appl. Phys.* **60**, 010101 (2021).
22. Zeng, Y. J. et al. Tuning quantum corrections and magnetoresistance in ZnO nanowires by ion implantation. *Nano Lett.* **12**, 666–672 (2012).
23. Fert, A. & Jaffrès, H. Conditions for efficient spin injection from a ferromagnetic metal into a semiconductor. *Phys. Rev. B* **64**, 184420 (2001).
24. Zhou, Y. et al. Investigating the origin of Fermi level pinning in Ge Schottky junctions using epitaxially grown ultrathin MgO films. *Appl. Phys. Lett.* **96**, 102103 (2010).
25. Ando, Y. et al. Comparison of nonlocal and local magnetoresistance signals in laterally fabricated  $\text{Fe}_3\text{Si}/\text{Si}$  spin-valve devices. *Appl. Phys. Express* **3**, 093001 (2010).
26. Tang, J. et al. Electrical spin injection and detection in  $\text{Mn}_5\text{Ge}_3/\text{Ge}/\text{Mn}_5\text{Ge}_3$  nanowire transistors. *Nano Lett.* **13**, 4036 (2013).
27. Panguluri, R. P. et al. Spin polarization and electronic structure of ferromagnetic  $\text{Mn}_5\text{Ge}_3$  epilayers. *Phys. Status Solidi B* **242**, R67 (2005).
28. Zeng, C. et al. Epitaxial ferromagnetic  $\text{Mn}_5\text{Ge}_3$  on Ge (111). *Appl. Phys. Lett.* **83**, 5002 (2003).
29. Li, H., Ruan, S. & Zeng, Y. J. Intrinsic van der Waals magnetic materials from bulk to the 2D limit: new frontiers of spintronics. *Adv. Mater.* **31**, 1900065 (2019).
30. Panda, J. et al. Ultimate spin currents in commercial chemical vapor deposited graphene. *ACS Nano* **14**, 12771–12780 (2020).
31. Mishra, H. et al. Experimental advances in charge and spin transport in chemical vapor deposited graphene. *J. Phys-Mater.* **4**, 042007 (2021).
32. Elphick, K. et al. Heusler alloys for spintronic devices: review on recent development and future perspectives. *Sci. Technol. Adv. Mat.* **22**, 235–271 (2021).
33. Jiang, S. & Yang, K. Review of high-throughput computational design of Heusler alloys. *J. Alloys Compd.* **867**, 158854 (2021).
34. Webster, P. J. Magnetic and chemical order in Heusler alloys containing cobalt and manganese. *J. Phys. Chem. Solids* **32**, 1221 (1971).
35. Graf, T., Felser, C. & Parkin, S. S. Simple rules for the understanding of Heusler compounds. *Prog. Solid. State Chem.* **39**, 1 (2011).
36. Tavares, S., Yang, K. & Meyers, M. A. Heusler alloys: Past, properties, new alloys, and prospects. *Prog. Mater. Sci.* **132**, 101017 (2023).
37. Felser, C. & Fecher, G. H. (eds) *Spintronics: from materials to devices*. (Springer, 2013).
38. Wurmehl, S. et al. The Heusler compound with highest Curie temperature and magnetic moment. *Appl. Phys. Lett.* **88**, 032503 (2006).
39. Galanakis, I., Dederichs, P. H. & Papanikolaou, N. Slater-Pauling behavior and origin of the half-metallicity of the full-Heusler alloys. *Phys. Rev. B* **66**, 174429 (2002).
40. Felser, C., Wollmann, L., Chadov, S., Fecher, G. H. & Parkin, S. S. Basics and prospective of magnetic Heusler compounds. *APL Mater.* **3**, 041518 (2015).
41. Hirohata, A. et al. Roadmap for emerging materials for spintronic device applications. *IEEE Trans. Magn.* **51**, 1 (2015).
42. Biswas, S. et al. Effect of disorder and strain on spin polarization of a  $\text{Co}_2\text{FeSi}$  Heusler alloy. *ACS Appl. Electron. Mater.* **3**, 4522–4534 (2021).
43. Geiersbach, U., Bergmann, A. & Westerholt, K. Preparation and structural properties of thin films and multilayers of the Heusler compounds  $\text{Cu}_2\text{MnAl}$ ,  $\text{Co}_2\text{MnSn}$ ,  $\text{Co}_2\text{MnSi}$  and  $\text{Co}_2\text{MnGe}$ . *Thin Solid Films* **425**, 225 (2003).
44. Soulen, R. J. et al. Measuring the spin polarization of a metal with a superconducting point contact. *Science* **282**, 85 (1998).
45. Kämmerer, S., Thomas, A., Hütten, A. & Reiss, G.  $\text{Co}_2\text{MnSi}$  Heusler alloy as magnetic electrodes in magnetic tunnel junctions. *Appl. Phys. Lett.* **85**, 79 (2004).
46. Dietl, T., Bonanni, A. & Ohno, H. Families of magnetic semiconductors—an overview. *J. Semicond.* **40**, 080301 (2019).
47. Wachter, P. Europium chalcogenides:  $\text{EuO}$ ,  $\text{EuS}$ ,  $\text{EuSe}$  and  $\text{EuTe}$ . *Handbook on the physics and chemistry of rare earths* **2**, 507 (1979).
48. Kasuya, T. & Yanase, A. Anomalous transport phenomena in Eu-chalcogenide alloys. *Rev. Mod. Phys.* **40**, 684 (1968).
49. Yuan, Y. et al. Nematicity of correlated systems driven by anisotropic chemical phase separation. *Phys. Rev. Mater.* **2**, 114601 (2018).
50. Ohno, H. et al. (Ga,Mn)As: a new diluted magnetic semiconductor based on GaAs. *Appl. Phys. Lett.* **69**, 363 (1996).
51. Dietl, T., Ohno, O. H., Matsukura, A. F., Cibert, J. & Ferrand, E. D. Zener model description of ferromagnetism in zinc-blende magnetic semiconductors. *Science* **287**, 1019 (2000).
52. MacDonald, A. H., Schiffer, P. & Samarth, N. Ferromagnetic semiconductors: moving beyond (Ga, Mn) As. *Nat. Mater.* **4**, 195 (2005).
53. Zhou, S. et al. Precise tuning of the Curie temperature of (Ga, Mn) As-based magnetic semiconductors by hole compensation: Support for valence-band ferromagnetism. *Phys. Rev. B* **94**, 075205 (2016).
54. Prucnal, S. et al. Band-gap narrowing in Mn-doped GaAs probed by room-temperature photoluminescence. *Phys. Rev. B* **92**, 224407 (2015).
55. Yuan, Y. et al. Interplay between localization and magnetism in (Ga, Mn)As and (In, Mn) As. *Phys. Rev. Mater.* **1**, 054401 (2017).
56. Mahadevan, P. & Zunger, A. Ferromagnetism in Mn-doped GaAs due to substitutional-interstitial complexes. *Phys. Rev. B* **68**, 075202 (2003).
57. Dong, S. et al. Carrier localization in quaternary  $\text{Ga}_{1-x}\text{Mn}_x\text{As}_{1-y}\text{P}_y$  ferromagnetic semiconductor films. *Phys. Rev. Mater.* **5**, 014402 (2021).
58. Prucnal, S., Rebohle, L. & Skorupa, W. Doping by flash lamp annealing. *Mater. Sci. Semicond. Process.* **62**, 115–127 (2017).
59. Birowska, M., Śliwa, C., Majewski, J. A. & Dietl, T. Origin of bulk uniaxial anisotropy in zinc-blende dilute magnetic semiconductors. *Phys. Rev. Lett.* **108**, 237203 (2012).
60. Wang, M. et al. Achieving high curie temperature in (Ga, Mn) As. *Appl. Phys. Lett.* **93**, 132103 (2008).
61. Xu, Q. et al. Room temperature ferromagnetism in ZnO films due to defects. *Appl. Phys. Lett.* **92**, 082508 (2008).
62. Stone, M. B. et al. Capping-induced suppression of annealing effects on  $\text{Ga}_{1-x}\text{Mn}_x\text{As}$  epilayers. *Appl. Phys. Lett.* **83**, 4568 (2003).
63. Kudrin, A. V. et al. High-temperature intrinsic ferromagnetism in heavily Fe-doped GaAs layers. *Semicond. Sci. Technol.* **35**, 125032 (2020).
64. Dietl, T. & Ohno, H. Dilute ferromagnetic semiconductors: Physics and spintronic structures. *Rev. Mod. Phys.* **86**, 187 (2014).
65. Ogawa, T., Shirai, M., Suzuki, N. & Kitagawa, I. First-principles calculations of electronic structures of diluted magnetic semiconductors (Ga,Mn)As. *J. Magn. Magn. Mater.* **196**, 428 (1999).
66. Piano, S. et al. Spin polarization of (Ga, Mn) As measured by Andreev spectroscopy: the role of spin-active scattering. *Phys. Rev. B* **83**, 081305 (2011).
67. Van Dorpe, P. et al. Very high spin polarization in GaAs by injection from a (Ga, Mn) As Zener diode. *Appl. Phys. Lett.* **84**, 3495–3497 (2004).

68. Johnston-Halperin, E. et al. Spin polarized Zener tunneling in (Ga, Mn) As. *Phys. Rev. B* **65**, 041306 (2002).
69. Nguyen, T. L. & Drouhin, H. J. Spin-current in a magnetic semiconductor tunnel junction: effect of external bias voltage. *Commun. Phys.* **32**, 413–413 (2022).
70. Spiesser, A. et al. Effect of thickness on structural and magnetic properties of  $\text{Mn}_5\text{Ge}_3$  films grown on Ge (111) by solid phase epitaxy. *Thin Solid Films* **518**, S113 (2010).
71. Forsyth, J. B. & Brown, P. J. The spatial distribution of magnetisation density in  $\text{Mn}_5\text{Ge}_3$ . *J. Condens. Matter Phys.* **2**, 2713 (1990).
72. Picozzi, S., Continenza, A. & Freeman, A. J. First-principles characterization of ferromagnetic  $\text{Mn}_5\text{Ge}_3$  for spintronic applications. *Phys. Rev. B* **70**, 235205 (2004).
73. Zeng, C., Zhu, W., Erwin, S. C., Zhang, Z. & Weitering, H. H. Initial stages of Mn adsorption on Ge (111). *Phys. Rev. B* **70**, 205340 (2004).
74. Ciszewski, R. Magnetic Structure of the  $\text{Mn}_5\text{Ge}_3$  Alloy. *Phys. Status Solidi B* **3**, 1999 (1963).
75. Forsyth, J. B. & Brown, P. J. *Proc. Int. Magnetism Conf. (Nottingham)*, p524 (1964).
76. Jackson, R. F., Scurlock, R. G., Utton, D. B. & Wray, E. M. The hyperfine fields at Mn in ferromagnetic  $\text{Mn}_5\text{Ge}_3$ . *Wray Proc. Phys. Soc.* **85**, 127 (1965).
77. Kalvig, R. et al. Hyperfine fields and anisotropy of the orbital moment in epitaxial  $\text{Mn}_5\text{Ge}_3$  films studied by  $^{55}\text{Mn}$  NMR. *Phys. Rev. B* **97**, 174428 (2018).
78. Olive-Mendez, S. et al. Epitaxial growth of  $\text{Mn}_5\text{Ge}_3/\text{Ge}(111)$  heterostructures for spin injection. *Thin Solid Films* **517**, 191 (2008).
79. Bechler, S. et al. Formation of  $\text{Mn}_5\text{Ge}_3$  by thermal annealing of evaporated Mn on doped Ge on Si (111). *Semicond. Sci. Technol.* **33**, 095008 (2018).
80. Spiesser, A. et al. Magnetic anisotropy in epitaxial  $\text{Mn}_5\text{Ge}_3$  films. *Phys. Rev. B* **86**, 035211 (2012).
81. Kalvig, R. et al. Ferromagnetic resonance in  $\text{Mn}_5\text{Ge}_3$  epitaxial films with weak stripe domain structure. *J. Phys. D Appl. Phys.* **50**, 125001 (2017).
82. Chen, T. Y., Chien, C. L. & Petrovic, C. Enhanced Curie temperature and spin polarization in  $\text{Mn}_4\text{FeGe}_3$ . *Appl. Phys. Lett.* **91**, 142505 (2007).
83. Reiff, W. M., Narasimhan, K. & Steinfink, H. Mössbauer and magnetic investigation of the system  $\text{Mn}_{5-x}\text{Fe}_x\text{Ge}_3$  ( $x = 0.5, 1.0$  and  $1.5$ ). *J. Solid State Chem.* **4**, 38 (1972).
84. Yamada, N., Shibasaki, S., Asai, K., Morii, Y. & Funahashi, S. Magnetic properties of  $(\text{Mn}_{1-x}\text{Te}_x)_5\text{Ge}_3$  ( $\text{Te} = \text{Cr}$  and  $\text{Fe}$ ). *Phys. B: Condens. Matter* **213**, 357 (1995).
85. Tegus, O., Bruck, E., De Boer, F. R. & Buschow, K. H. J. Magnetic and magnetocaloric properties of  $\text{Mn}_5\text{Ge}_{3-x}\text{Sb}_x$ . *J. Alloys Compd.* **337**, 269 (2002).
86. Michez, L. A. et al. Unveiling the atomic position of C in  $\text{Mn}_5\text{Ge}_3\text{C}_x$  thin films. *Phys. Rev. Mater.* **6**, 074404 (2022).
87. Kalvig, R., Jedryka, E., Wojcik, M., Petit, M. & Michez, L. Selective modification of the unquenched orbital moment of manganese introduced by carbon dopant in epitaxial  $\text{Mn}_5\text{Ge}_3\text{C}_{0.2}/\text{Ge}(111)$  films. *Phys. Rev. B* **101**, 094401 (2020).
88. Spiesser, A. et al. Control of magnetic properties of epitaxial  $\text{Mn}_5\text{Ge}_3\text{C}_x$  films induced by carbon doping. *Phys. Rev. B* **84**, 165203 (2011).
89. Slipukhina, I., Arras, E., Mavropoulos, P. & Pochet, P. Simulation of the enhanced Curie temperature in  $\text{Mn}_5\text{Ge}_3\text{C}_x$  compounds. *Appl. Phys. Lett.* **94**, 192505 (2009).
90. Kalvig, R., Jedryka, E., Wojcik, M., Petit, M. & Michez, L. Highly ordered carbon penetration into the  $\text{Mn}_5\text{Ge}_3\text{C}_x$  lattice: A superstructure in  $\text{Mn}_5\text{Ge}_3\text{C}_{0.5}$  inferred from a Mn  $^{55}\text{Mn}$  NMR study. *Phys. Rev. B* **105**, 094405 (2022).
91. Sangaletti, L. et al. Atomic approach to core-level spectroscopy of delocalized systems: Case of ferromagnetic metallic  $\text{Mn}_5\text{Ge}_3$ . *Phys. Rev. B* **81**, 085204 (2010).
92. Grytzelius, J. H., Zhang, H. M. & Johansson, L. S. O. Surface atomic and electronic structure of  $\text{Mn}_5\text{Ge}_3$  on Ge (111). *Phys. Rev. B* **84**, 195306 (2011).
93. Ndiaye, W. et al. Bulk electronic structure of  $\text{Mn}_5\text{Ge}_3/\text{Ge}(111)$  films by angle-resolved photoemission spectroscopy. *Phys. Rev. B* **87**, 165137 (2013).
94. Dedkov, Y. S., Holder, M., Mayer, G., Fonin, M. & Preobrajenski, A. B. Spin-resolved photoemission of a ferromagnetic  $\text{Mn}_5\text{Ge}_3$  (0001) epilayer on Ge (111). *J. Appl. Phys.* **105**, 073909 (2009).
95. Ndiaye, W. et al. k dependence of the spin polarization in  $\text{Mn}_5\text{Ge}_3/\text{Ge}(111)$  thin films. *Phys. Rev. B* **91**, 125118 (2015).
96. Abbes, O., Portavoce, A., LeThanh, V., Girardeaux, C. & Michez, L. Phase formation during Mn thin film reaction with Ge: Self-aligned germanide process for spintronics. *Appl. Phys. Lett.* **103**, 172405 (2013).
97. Alvidrez-Lechuga, A., Antón, R. L., Holguín-Momaca, J. T., Espinosa-Magaña, F. & Olive-Méndez, S. F. Role of the substrate temperature on the growth of  $\text{Mn}_5\text{Ge}_3$  thin films by co-deposition of Mn and Ge on Ge (001) substrates by magnetron sputtering. *Thin Solid Films* **616**, 111 (2016).
98. LeThanh, V. et al. Epitaxial growth and magnetic properties of  $\text{Mn}_5\text{Ge}_3/\text{Ge}$  and  $\text{Mn}_5\text{Ge}_3\text{C}_x/\text{Ge}$  heterostructures for spintronic applications. *Adv. Nat. Sci. Nanosci.* **4**, 043002 (2013).
99. Kim, H. et al. Epitaxial  $\text{Mn}_5\text{Ge}_3$  nano-islands on a Ge (001) surface. *Nanotechnology* **19**, 025707 (2007).
100. Olive Méndez, S. F., Michez, L. A., Spiesser, A. & LeThanh, V. Epitaxial growth of strained  $\text{Mn}_5\text{Ge}_3$  nanoislands on Ge (001). *Phys. Status Solidi B* **252**, 1854 (2015).
101. Xie, Y. et al. Epitaxial  $\text{Mn}_5\text{Ge}_3$  (100) layer on Ge (100) substrates obtained by flash lamp annealing. *Appl. Phys. Lett.* **113**, 222401 (2018).
102. Xie, Y. et al. Strain-induced switching between noncollinear and collinear spin configuration in magnetic  $\text{Mn}_5\text{Ge}_3$  films. *Phys. Rev. B* **104**, 064416 (2021).
103. Xie, Y. et al. Influence of fabrication parameters on the magnetic and structural properties of  $\text{Mn}_5\text{Ge}_3$ . *Semicond. Sci. Technol.* **37**, 065009 (2022).
104. Fischer, I. A. et al. Hanle-effect measurements of spin injection from  $\text{Mn}_5\text{Ge}_3\text{C}_{0.8}/\text{Al}_2\text{O}_3$ -contacts into degenerately doped Ge channels on Si. *Appl. Phys. Lett.* **105**, 222408 (2014).
105. Elahi, E. et al. Recent innovations in 2D magnetic materials and their potential applications in the modern era. *Mater. Today* **72**, 183–206 (2024).
106. Zhang, L., Zhou, J., Li, H., Shen, L. & Feng, Y. P. Recent progress and challenges in magnetic tunnel junctions with 2D materials for spintronic applications. *Appl. Phys. Rev.* **8**, 021308 (2021).
107. Ahn, E. C. 2D materials for spintronic devices. *npj 2D Mater. Appl.* **4**, 17 (2020).
108. Jiang, X. et al. Recent progress on 2D magnets: Fundamental mechanism, structural design and modification. *Appl. Phys. Rev.* **8**, 031305 (2021).
109. Kuo, C. T., Neumann, M. & Balamurugan, K. Exfoliation and Raman spectroscopic fingerprint of few-Layer  $\text{NiPS}_3$  van der Waals crystals. *Sci. Rep.* **6**, 20904 (2016).
110. Du, K. Z. et al. Wide-Range Band Gap, and Raman Study on Ultrathin Layers of Metal Phosphorus Trichalcogenides. *ACS Nano* **10**, 1738–1743 (2016).
111. Lee, J. U. et al. Ising-type magnetic ordering in atomically thin  $\text{FePS}_3$ . *Nano Lett.* **16**, 7433–7438 (2016).
112. Huang, B. et al. Layer-dependent ferromagnetism in a van der Waals crystal down to the monolayer limit. *Nature* **546**, 270–273 (2017).



113. Gong, C. et al. Discovery of intrinsic ferromagnetism in two-dimensional van der Waals crystals. *Nature* **546**, 265–269 (2017).
114. Deng, Y. et al. Gate-tunable room-temperature ferromagnetism in two-dimensional  $\text{Fe}_3\text{GeTe}_2$ . *Nature* **563**, 94–99 (2018).
115. Papavasileiou, A. V. et al. Ferromagnetic elements in two-dimensional materials: 2D magnets and beyond. *Adv. Funct. Mater.* **34**, 2309046 (2024).
116. Kim, H. H. et al. Evolution of interlayer and intralayer magnetism in three atomically thin chromium trihalides. *Proc. Natl. Acad. Sci. USA* **116**, 11131–11136 (2019).
117. Fei, Z. et al. Two-dimensional itinerant ferromagnetism in atomically thin  $\text{Fe}_3\text{GeTe}_2$ . *Nat. Mater.* **17**, 778–782 (2018).
118. Zhang, G. et al. Above-room-temperature strong intrinsic ferromagnetism in 2D van der Waals  $\text{Fe}_3\text{GaTe}_2$  with large perpendicular magnetic anisotropy. *Nat. Commun.* **13**, 5067 (2022).
119. Bonilla, M. et al. Strong room-temperature ferromagnetism in  $\text{VSe}_2$  monolayers on van der Waals substrates. *Nat. Nanotech.* **13**, 289–293 (2018).
120. O'Hara, D. J. et al. Room temperature intrinsic ferromagnetism in epitaxial manganese selenide films in the monolayer limit. *Nano Lett* **18**, 3125–3131 (2018).
121. Wang, X. et al. Ferromagnetism in 2D vanadium diselenide. *ACS Nano* **15**, 16236–16241 (2021).
122. Wang, F. et al. New frontiers on van der Waals layered metal phosphorous trichalcogenides. *Adv. Funct. Mater.* **28**, 1802151 (2018).
123. Yan, S. et al. First-principles study of magnetic interactions and excitations in antiferromagnetic van der Waals material  $\text{MPX}_3$  (M = Mn, Fe, Co, Ni; X = S, Se). *J. Phys.-Condes. Matter* **36**, 065502 (2023).
124. Bhutani, A. et al. Strong anisotropy in the mixed antiferromagnetic system  $\text{Mn}_{1-x}\text{Fe}_x\text{PSe}_3$ . *Phys. Rev. Mater.* **4**, 034411 (2020).
125. Basnet, R. et al. Understanding and Tuning Magnetism in Layered Ising-Type Antiferromagnet  $\text{FePSe}_3$  for Potential 2D Magnet. *Adv. Electron. Mater.* **10**, 2300738 (2024).
126. Li, X. et al. Spin-dependent transport in van der Waals magnetic tunnel junctions with  $\text{Fe}_3\text{GeTe}_2$  electrodes. *Nano Lett* **19**, 5133–5139 (2019).
127. Kim, D. et al. Antiferromagnetic coupling of van der Waals ferromagnetic  $\text{Fe}_3\text{GeTe}_2$ . *Nanotechnology* **30**, 245701 (2019).
128. Hu, C. et al. From two- to multi-state vertical spin valves without spacer layer based on  $\text{Fe}_3\text{GeTe}_2$  van der Waals homo-junctions. *Sci. Bull.* **65**, 1072–1077 (2020).
129. Zhuang, H. L., Kent, P. R. C. & Hennig, R. G. Strong anisotropy and magnetostriiction in the two-dimensional Stoner ferromagnet  $\text{Fe}_3\text{GeTe}_2$ . *Phys. Rev. B* **93**, 134407 (2016).
130. Min, K. H. et al. Tunable spin injection and detection across a van der Waals interface. *Nat. Mater.* **21**, 1144–1149 (2022).
131. León-Brito, N., Bauer, E. D., Ronning, F., Thompson, J. D. & Movshovich, R. Magnetic microstructure and magnetic properties of uniaxial itinerant ferromagnet  $\text{Fe}_3\text{GeTe}_2$ . *J. Appl. Phys.* **120**, 083903 (2016).
132. Tan, C. et al. Hard magnetic properties in nanoflake van der Waals  $\text{Fe}_3\text{GeTe}_2$ . *Nat. Commun.* **9**, 1554 (2018).
133. Zhang, L. et al. Substrate-modulated ferromagnetism of two-dimensional  $\text{Fe}_3\text{GeTe}_2$ . *Appl. Phys. Lett.* **116**, 042402 (2020).
134. Seo, J. et al. Nearly room temperature ferromagnetism in a magnetic metal-rich van der Waals metal. *Sci. Adv.* **6**, 8912 (2020).
135. Liu, S. et al. Wafer-scale two-dimensional ferromagnetic  $\text{Fe}_3\text{GeTe}_2$  thin films grown by molecular beam epitaxy. *npj 2. D Mater. Appl.* **1**, 30 (2017).
136. Liu, S. et al. Tuning 2D magnetism in  $\text{Fe}_{3+x}\text{GeTe}_2$  films by element doping. *Natl. Sci. Rev.* **9**, 117 (2022).
137. Tian, C. K. et al. Domain wall pinning and hard magnetic phase in Co-doped bulk single crystalline  $\text{Fe}_3\text{GeTe}_2$ . *Phys. Rev. B* **99**, 184428 (2019).
138. Zhang, J. et al. Enhanced magnetic and electrical properties of Co-doped  $\text{Fe}_3\text{GeTe}_2$ . *Appl. Phys. Lett.* **124**, 103103 (2024).
139. Wang, Z. et al. Tunneling spin valves based on  $\text{Fe}_3\text{GeTe}_2/\text{hBN}/\text{Fe}_3\text{GeTe}_2$  van der Waals heterostructures. *Nano Lett* **18**, 4303–4308 (2018).
140. Zhou, L. et al. Gate-tunable spin valve effect in  $\text{Fe}_3\text{GeTe}_2$ -based van der Waals heterostructures. *InfoMat* **5**, e12371 (2023).
141. He, X. et al. Nonlocal spin valves based on Graphene/ $\text{Fe}_3\text{GeTe}_2$  van der Waals heterostructures. *ACS Appl. Mater. Interfaces* **15**, 9649–9655 (2023).
142. Chen, C. et al. Air-stable 2D  $\text{Cr}_5\text{Te}_8$  nanosheets with thickness-tunable ferromagnetism. *Adv. Mater.* **34**, 2107512 (2022).
143. Kumar, P. et al. Magnetic imaging with spin defects in hexagonal boron nitride. *Phys. Rev. Appl.* **18**, L061002 (2022).
144. Sanvito, S. et al. Accelerated discovery of new magnets in the Heusler alloy family. *Sci. Adv.* **3**, e1602241 (2017).
145. Yamada, A. et al. Growth of all-epitaxial  $\text{Co}_2\text{MnSi}/\text{Ge}/\text{Co}_2\text{MnSi}$  vertical spin-valve structures on Si. *Mater. Sci. Semicond. Process.* **173**, 108140 (2024).
146. Hirohata, A. & Lloyd, D. C. Heusler alloys for metal spintronics. *MRS Bull* **47**, 593–599 (2022).
147. Dietl, T. A ten-year perspective on dilute magnetic semiconductors and oxides. *Nat. Mater.* **9**, 965–974 (2010).
148. Yan, Z., Gao, R., Chang, M., Qi, S. & Xu, X. Dramatically enhanced carrier mobility and Curie temperature in np codoped ZnO by proximity effect. *J. Magn. Magn. Mater.* **496**, 165966 (2020).
149. Lee, Y. H. Is it possible to create magnetic semiconductors that function at room temperature? *Science* **382**, adl0823 (2023).
150. Wu, J. et al. Room-Temperature Ferromagnetism and Fermi Level Pinning in Multilayer Graphene Films Derived from Ferrocene. *Adv. Funct. Mater.* **34**, 2312119 (2024).
151. Dankert, A., Langouche, L., Kamalakar, M. V. & Dash, S. P. High-performance molybdenum disulfide field-effect transistors with spin tunnel contacts. *ACS nano* **8**, 476–482 (2014).
152. Kamalakar, M. V., Madhushankar, B. N., Dankert, A. & Dash, S. P. Low Schottky Barrier Black Phosphorus Field-Effect Devices with Ferromagnetic Tunnel Contacts. *Small* **11**, 2209–2216 (2015).
153. Dayen, J. F., Ray, S. J., Karis, O., Vera-Marun, I. J. & Kamalakar, M. V. Two-dimensional van der Waals spinterfaces and magnetic-interfaces. *Appl. Phys. Rev.* **7**, 011303 (2020).
154. Otani, Y., Shiraishi, M., Oiwa, A., Saitoh, E. & Murakami, S. Spin conversion on the nanoscale. *Nat. Phys.* **13**, 829–832 (2017).
155. Soumyanarayanan, A., Reyren, N., Fert, A. & Panagopoulos, C. Emergent phenomena induced by spin-orbit coupling at surfaces and interfaces. *Nature* **539**, 509–517 (2016).
156. Hoffmann, A. Spin Hall effects in metals. *IEEE Trans. Magn.* **49**, 5172–5193 (2013).
157. Yamada, S. et al. Half-Metallic Heusler Alloy/GaN Heterostructure for Semiconductor Spintronics Devices. *Adv. Electron. Mater.* **9**, 2300045 (2023).
158. Hamaya, K. et al. Estimation of the spin polarization for Heusler-compound thin films by means of nonlocal spin-valve measurements: Comparison of  $\text{Co}_2\text{FeSi}$  and  $\text{Fe}_3\text{Si}$ . *Phys. Rev. B* **85**, 100404 (2012).
159. Zhao, B. et al. A Room-Temperature Spin-Valve with van der Waals Ferromagnet  $\text{Fe}_5\text{GeTe}_2/\text{Graphene}$  Heterostructure. *Adv. Mater.* **35**, 2209113 (2023).
160. Saito, Y. et al. Spin-based MOSFETs for logic and memory applications and spin accumulation signals in CoFe/tunnel barrier/SOI devices. *IEEE Trans. Magn.* **48**, 2739–2745 (2012).

## Acknowledgements

This work was supported by the National Natural Science Foundation of China (52273298, 12304143, and 12274182), and the Shenzhen

Science and Technology Program (JCYJ20210324095611032, and JCYJ20220818100008016). Y.Y. acknowledges the support from the Innovation/Entrepreneurship Program of Jiangsu Province (JSSCTD202146 and JSSCRC2021538). Y.X. acknowledges the support from the Post-doctoral Overseas Talent Recruitment Special Program of Ministry of Education of China and Research Foundation of Jiangsu university (22JDG043).

### Author contributions

Y.X. wrote the main text and prepared figures. Y.Z. conceived the project. All of the authors revised the manuscript and participated in discussions.

### Competing interests

The authors declare no competing interests.

### Additional information

**Correspondence** and requests for materials should be addressed to Yu-Jia Zeng.

**Reprints and permissions information** is available at <http://www.nature.com/reprints>

**Publisher's note** Springer Nature remains neutral with regard to jurisdictional claims in published maps and institutional affiliations.

**Open Access** This article is licensed under a Creative Commons Attribution-NonCommercial-NoDerivatives 4.0 International License, which permits any non-commercial use, sharing, distribution and reproduction in any medium or format, as long as you give appropriate credit to the original author(s) and the source, provide a link to the Creative Commons licence, and indicate if you modified the licensed material. You do not have permission under this licence to share adapted material derived from this article or parts of it. The images or other third party material in this article are included in the article's Creative Commons licence, unless indicated otherwise in a credit line to the material. If material is not included in the article's Creative Commons licence and your intended use is not permitted by statutory regulation or exceeds the permitted use, you will need to obtain permission directly from the copyright holder. To view a copy of this licence, visit <http://creativecommons.org/licenses/by-nc-nd/4.0/>.

© The Author(s) 2025